UNIVERSITY OF OKLAHOMA

GRADUATE COLLEGE

HEAT AND MOISTURE TRANSPORT DYNAMICS WITHIN THE CONVECTIVE BOUNDARY LAYER: INSIGHTS FROM THE SOUTHERN GREAT PLAINS ARM SITE

A THESIS

SUBMITTED TO THE GRADUATE FACULTY

in partial fulfillment of the requirements for the

Degree of

MASTER OF SCIENCE

By

LEIA M. OTTERSTATTER
Norman, Oklahoma
2025

Downloaded from SHAREOK. Persistent Handle URL: https://hdl.handle.net/11244/341620

HEAT AND MOISTURE TRANSPORT DYNAMICS WITHIN THE CONVECTIVE BOUNDARY LAYER: INSIGHTS FROM THE SOUTHERN GREAT PLAINS ARM SITE

A THESIS APPROVED FOR THE SCHOOL OF METEOROLOGY

BY THE COMMITTEE CONSISTING OF

Dr. Scott Salesky (Chair)

Dr. Otavio Acevedo

Dr. Tyler Bell

© Copyright by LEIA M. OTTERSTATTER 2025
All Rights Reserved.

Acknowledgments

First and foremost, I want to thank my mom, Linda, for her endless love, support, guidance, and encouragement. She has been the foundation of everything I've accomplished, not only as a scientist but as a person. Through every challenge, late-night call (or Facetime), and moment of doubt, she has been by my side. I truly wouldn't be here without her, and I am forever grateful.

A huge thank you to my research advisor, Dr. Scott Salesky, and my research mentor, Dr. Brian Greene, two people who introduced me to the world of boundary layer research. I would also like to thank Dr. Madeline Frank who mentored and helped me succeed in this research field. Scott, your guidance and enthusiasm for boundary layer meteorology have made this journey incredibly rewarding. Brian and Maddie, your mentorship and encouragement have meant the world to me, and I am incredibly thankful for your support along the way. A special thank you to Rob Newsom at the Pacific Northwest National Laboratory (PNNL) for assistance with data selection and gathering.

And of course, I have to thank Sylvie, my little four-legged research assistant. She may not understand the complexities of meteorology, but she definitely knows when I need a break or when it's time to go to bed. Whether it was curling up next to me during long coding or writing sessions, nudging me outside for some fresh air, or just being her funny, loving self; she made the tough days easier and the good days even better.

This thesis would not have been possible without the unwavering support, encouragement, and kindness of so many amazing people (and one truly exceptional dog). I am truly thankful for each and every one of you and I am sincerely appreciative of all the support I've received along the way.

This work is supported by the U.S. Department of Energy Atmospheric System Research Program, Grant #DE-SC0022124.

Table of Contents

Acknowledgments **iv**

List Of Tables **vii**

List Of Figures **viii**

Abstract **xi**

1 Introduction **1**
1.1 Atmospheric Boundary Layer Overview 1
1.2 Motivation & Scientific Importance 3
1.3 Research Gap & Questions 8

2 Background & Literature Review **11**
2.1 LSMs, Coherent Structures, and Their Role in Turbulence 11
2.2 Mixed-Layer Similarity Theory 14
2.3 Parameter Framework for the Moist CBL 17

3 Data & Methodology **20**
3.1 Data Sources 20
3.2 Instrumentation & Measurements 24
3.2.1 Total Sky Imager (TSI) 24
3.2.2 Doppler Lidar (DL) 25
3.2.3 Eddy Correlation (ECOR) System 27
3.2.4 Atmospheric Boundary Layer Depth (z_i) 29
3.2.5 Raman Lidar (RL) 30
3.3 Data Preprocessing & Selection Criteria 31
3.4 Analysis Methods 36

4 Results **45**
4.1 Time-Height Structure of Heat and Moisture Transport 45
4.2 Vertical Structure of Scalar Variability 46
4.2.1 Vertical Velocity Variance 48
4.2.2 Moisture Variance 51
4.2.3 Temperature Variance 53
4.2.4 Temperature-Humidity Covariance 56
4.3 Spectral Characteristics of Vertical Velocity Fluctuations 59

4.4 Spectral Characteristics of Heat and Moisture Fluctuations 63
4.4.1 Composite Mean Spectrograms of Temperature and Humidity 63
4.4.2 Temperature Spectral Analysis by Stability Regime 65
4.4.3 Moisture Spectral Analysis by Stability Regime 69

5 Summary and Conclusions **74**
5.1 Future Work 77

Reference List **80**

Appendix **83**
1 Appendix 83

List Of Tables

3.1 Summary of Southern Great Plains (SGP) Atmospheric Radiation Measurement (ARM) observational datasets used in this study, including data type, ARM product name, temporal and spatial resolutions, and the primary variables used from each product. 23

A.1 Summary of Highly Unstable Cases 83
A.2 Summary of Moderately Unstable Cases 85
A.3 Summary of Weakly Unstable Cases 86

List Of Figures

1.1 The boundary layer typically includes three main parts: a highly turbulent mixed layer near the surface, a residual layer above that containing remnants of the previous day's mixed-layer air, and a stable boundary layer that forms overnight with intermittent turbulence. The mixed layer itself is often divided into a subcloud layer and an overlying cloud layer (adapted from Stull 1988). 2

1.2 Conceptual schematic of wall-bounded turbulence from Marusic et al. (2010). (Left) Layered structure of the turbulent boundary layer, with increasing eddy size from wall to outer region. (Top-middle) Streamwise-aligned VLSMs that can extend over 15 to 20 boundary layer thicknesses. (Top-right) Scale decomposition of velocity fluctuations showing modulation of small-scale activity by large-scale motions. (Bottom) Side view of near-wall coherent structures producing alternating streaks. 6

3.1 Map highlighting Oklahoma and Kansas with orange markers indicating locations of all SGP facilities. 20

3.2 Map of Oklahoma with red star indicating location of the SGP ARM site in Lamont, Oklahoma. 21

3.3 Labeled image of the Total Sky Imager. Image provided by ARM TSI Handbook (Morris 2005). 25

3.4 Labeled image of Doppler Lidar. Image provided by ARM DL Handbook (Newsom & Krishnamurthy 2022). 26

3.5 Time–height cross-section of mean zonal wind ($\bar{u}$) from Doppler lidar measurements on May 18, 2018, between 15:00–16:00 UTC. The color shading indicates the magnitude of $\bar{u}$ (m/s), with negative values representing westerly flow. Dashed black lines mark selected altitudes within the boundary layer where zonal winds are averaged for further analysis. Mean values of $\bar{u}$ at these levels are annotated directly on the plot. . . 27

3.6 Change of ABL depth over 24 hours. The blue line indicates raw z_i data and red dots show calculated 1-hour averages of z_i. 30

3.7 Labeled image of Raman Lidar. Image provided by ARM RL Handbook (Newsom et al. 2022). 31

3.8 Histogram of Obukhov Length (L) for the final 107 cases. 33

3.9 Histogram of boundary layer depth (z_i) for the final 107 cases after filtering. 34

3.10 Histogram of global stability parameter ($-z_i/L$) for the final 107 cases. 35

3.11 Distribution of the global stability parameter ($-z_i/L$) across observed cases. The dataset is categorized into three regimes: weakly unstable ($0 < -z_i/L \leq 10$, blue), moderately unstable ($10 < -z_i/L \leq 50$, orange), and highly unstable ($-z_i/L > 50$, red). The histogram illustrates the frequency of occurrences within each regime, highlighting the transition from shear- to buoyancy-dominated turbulence. 37

3.12 Distribution of Obukhov length (L) across observed cases, grouped by stability regime. Weakly unstable (13 cases, blue), moderately unstable (36 cases, orange), and highly unstable (58 cases, red). 38

3.13 Histograms of Bowen ratio (left) and evaporative fraction (E_f, right) for 107 observed cases. 40

3.14 Time-Height profiles of vertical velocity (top), temperature (middle), and water vapor mixing ratio (bottom) for August 1, 2018, at the SGP Central Facility. 41

3.15 Radial velocity plotted against intensity, illustrating the relationship between the two variables. The red line indicates the defined floor level, serving as a reference point for the data. 42

4.1 Joint probability density function (PDF) of evaporative fraction (E_f) and global stability parameter ($-z_i/L$) for the final 107 cases. Marginal histograms show the individual distributions of each variable. 46

4.2 Normalized vertical velocity variance profiles $\overline{w'w'}/w_*^2$ as a function of normalized height z/z_i across three instability regimes. Individual lines represent hourly cases (top); shaded regions denote one and two standard deviations from the composite mean (bottom). 48

4.3 Normalized composite mean vertical velocity variance profiles for highly, moderately, and least unstable cases. 49

4.4 As in Fig. 4.2, but for normalized moisture flux profiles $\overline{q'q'}/q_*^2$ as a function of normalized height z/z_i across three instability regimes. . . . 51

4.5 As in Fig. 4.3, but for moisture variance. 52

4.6 As in Fig. 4.2, but for normalized temperature flux profiles $\overline{\theta'\theta'}/\theta_*^2$ as a function of normalized height z/z_i across three instability regimes. . . . 54

4.7 As in Fig. 4.3, but for temperature variance. 55

4.8 As in Fig. 4.2, but for normalized temperature–humidity flux profiles, $\overline{\theta'q'}/\theta_* q_*$, as a function of normalized height z/z_i across three instability regimes. 56

4.9 As in Fig. 4.3, but for temperature–humidity variance. 58

4.10 Schematic illustrating the spectral domain used for analysis of turbulent motions in the CBL. The y-axis shows the normalized wavelength (λ/z_i), with $\lambda/z_i > 1$ representing LSMs and $\lambda/z_i < 1$ representing small-scale motions (SSMs). The x-axis denotes normalized height (z/z_i). The dashed line at $\lambda/z_i = 1$ separates contributions from LSMs and SSMs while indicating the scale of the CBL. Arrows indicate increasing scale (vertical) and increasing height (horizontal) within the CBL. 60
4.11 Composite mean spectrograms of vertical velocity for all cases, excluding outliers. Non-dimensional height (z/z_i) is on the x-axis, and non-dimensional wavelength (λ/z_i) is on the y-axis. Color shading indicates spectral power. 61
4.12 Composite mean spectrograms of vertical velocity variance for highly (top), moderately (middle), and weakly unstable (bottom) regimes. The x-axis shows non-dimensional height (z/z_i) and the y-axis shows non-dimensional wavelength (λ/z_i). Color shading indicates spectral power. 62
4.13 Composite mean spectrograms of temperature (left) and humidity (right) for all cases, excluding outliers. Non-dimensional height (z/z_i) is on the x-axis, and non-dimensional wavelength (λ/z_i) is on the y-axis. Color shading indicates spectral power. 64
4.14 Composite mean spectrograms of temperature variance for highly (top), moderately (middle), and weakly unstable (bottom) regimes. The x-axis shows non-dimensional height (z/z_i) and the y-axis shows non-dimensional wavelength (λ/z_i). Color shading indicates spectral power. 66
4.15 Composite mean spectrograms of temperature fluctuations based on dominant modes of E_f, ranging from (top) 0 to 0.3, (middle) 0.3 to 0.7, and (bottom) 0.7 to 1.0. 68
4.16 Composite mean spectrograms of humidity fluctuations for highly (top), moderately (middle), and weakly unstable (bottom) cases, as in Figure 4.14. 70
4.17 Composite mean spectrograms of humidity fluctuations based on dominant modes of E_f, ranging from (top) 0 to 0.3, (middle) 0.3 to 0.7, and (bottom) 0.7 to 1.0. 72

Abstract

Increasing our understanding of moisture transport within the convective boundary layer (CBL) is crucial for improving weather and climate forecasting. Turbulent moisture fluxes within the CBL are critical for precipitation, cloud formation, the surface energy budget, and the initiation of deep convection. Despite the importance of moisture transport, most previous studies have focused on dry CBLs in the absence of humidity. Furthermore, the transport of moisture and other scalars such as temperature can be highly dissimilar, with their statistics largely determined by their respective entrainment zone structure. Thus, many aspects of moisture transport in the CBL remain poorly understood.

This study aims to address two key research questions: (1) How do moisture-related processes influence vertical profiles of turbulent statistics in the CBL? (2) Do large-scale turbulent motions (turbulent flows in the CBL that span the entire boundary layer depth or more) exhibit similar spectral properties for temperature and humidity? Using high-resolution Doppler lidar, Raman lidar, and eddy correlation flux measurements from the U.S. Department of Energy (DOE) Southern Great Plains (SGP) Atmospheric Radiation Measurement (ARM) site in Lamont, Oklahoma, collected during summer 2018, we analyzed the data as a function of global stability (quantified by $-z_i/L$) and evaporative fraction (E_f, a parameter not accounted for in classical mixed-layer similarity theory). Results show that moisture fluctuations are generally more vertically confined than temperature and are sensitive to surface evaporative conditions. Spectral analysis reveals that temperature variance is dominated by LSMs spanning the boundary layer depth, whereas humidity variance is concentrated at smaller scales and lower altitudes. These findings highlight differences in scalar transport mechanisms and emphasize the importance of incorporating humidity-specific entrainment and large-scale variability in turbulence parameterizations to improve weather and climate models.

Chapter 1

Introduction

1.1 Atmospheric Boundary Layer Overview

The Atmospheric Boundary Layer (ABL) is the lowest portion of the atmosphere, typically extending up to 1-2 km, and is directly influenced by the Earth's surface on timescales of an hour or less (Stull 1988). This layer plays a critical role in the vertical exchange of heat, moisture, and momentum between the surface and the free atmosphere (Kaimal & Finnigan 1994). The structure and evolution of the ABL are governed by diurnal variability and modulated by surface forcings such as net radiation, surface heat fluxes, and soil moisture, and large-scale factors, including cloud cover and geostrophic wind, which influence wind shear and boundary-layer dynamics.

Within the ABL, the convective boundary layer (CBL) arises during the daytime when surface heating generates buoyant plumes that initiate turbulent mixing. This turbulence, primarily driven by surface buoyancy, promotes vertical redistribution of heat, moisture, and momentum. The structure of turbulence in the CBL is influenced by surface heating, atmospheric instability, and vertical wind shear, all of which govern the intensity and organization of turbulent motions (Sorbjan 1989). This makes the CBL a crucial region for understanding weather and climate processes. Accurate representation of these turbulent dynamics is vital for numerical weather prediction and climate modeling, particularly in modeling the surface fluxes and cloud development.

As the sun rises and heats the surface, the air near the ground becomes warmer and less dense, initiating upward motion. These buoyant thermals rise through the mixed layer and entrain drier, more stable air from above the capping inversion, deepening the boundary layer throughout the day. The entrainment zone (EZ) forms at the top of the CBL, where turbulent thermals overshoot into the stably stratified free atmosphere and subsequently mix downward. The EZ is the layer at the top of the mixed layer where buoyant updrafts extend into the overlying stable air, driving mixing and entrainment processes (Fowler 2006). This entrainment process is central to the growth and evolution of the CBL and plays a critical role in the vertical transport of scalars such as temperature and humidity (Fedorovich et al. 2004). Figure 1.1 illustrates the evolution of the ABL throughout this process, highlighting the growth of the CBL and the development of the EZ over time.

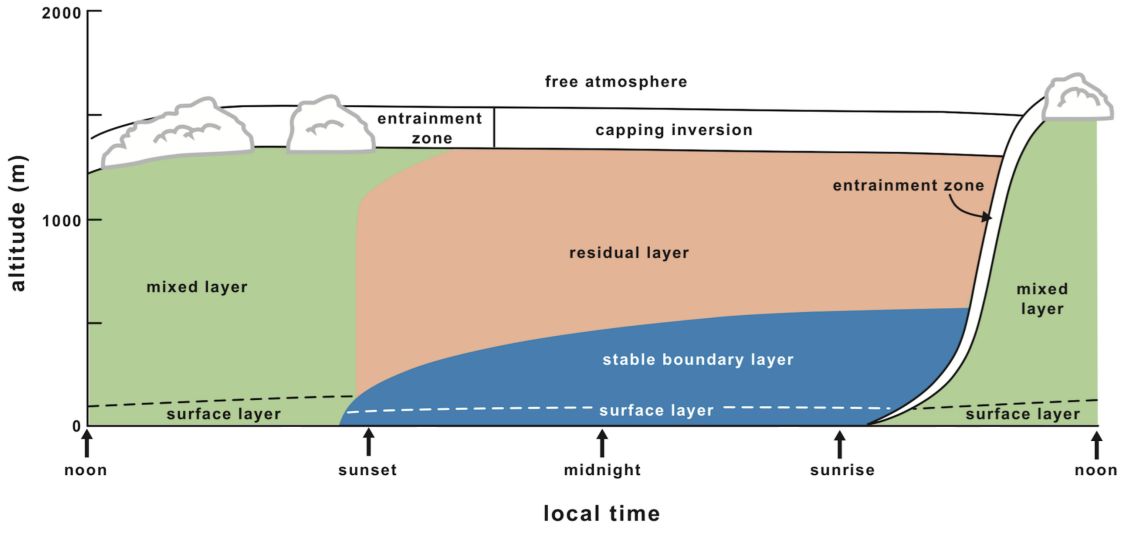

Figure 1.1: The boundary layer typically includes three main parts: a highly turbulent mixed layer near the surface, a residual layer above that containing remnants of the previous day's mixed-layer air, and a stable boundary layer that forms overnight with intermittent turbulence. The mixed layer itself is often divided into a subcloud layer and an overlying cloud layer (adapted from Stull 1988).

Foundational parameterizations, such as those developed by Deardorff (1972), Louis (1979), and Beljaars (1995), have aimed to capture these processes in numerical models. These schemes account for stability-dependent mixing and turbulent fluxes that emerge under convective conditions. Despite these advances, the interactions between turbulence, surface fluxes, and entrainment processes are poorly understood and remain a topic of active research.

1.2 Motivation & Scientific Importance

The accurate prediction of turbulent fluxes of momentum, heat, and moisture in the CBL is critical for understanding land-atmosphere interactions, surface energy exchanges, the hydrological cycle, and the structure of the boundary layer itself. Micrometeorological methods, such as eddy covariance, have been widely used to quantify turbulent exchanges of heat, moisture, and momentum (Baldocchi et al. 1988; Moncrieff et al. 1997). These approaches provide essential insights into land-atmosphere interactions, supporting observational studies, like this work. In particular, understanding the transport of heat and moisture within the CBL is vital for improving our ability to predict precipitation, cloud formation, and surface energy budgets, all of which play a fundamental role in weather and climate systems.

Moreover, moisture transport directly influences CBL dynamics through its effect on buoyancy. The buoyancy term in the Navier–Stokes equations is typically expressed using the virtual potential temperature, θ_v, as

$$B = \frac{g}{\Theta_0} \left(\theta_v - \overline{\theta_v} \right), \tag{1.1}$$

where B is the buoyancy acceleration (m s^{-2}), g is the gravitational acceleration (9.81 m s^{-2}), Θ_0 is a reference potential temperature (K), θ_v is the local virtual potential temperature (K), and $\overline{\theta_v}$ is the horizontal mean of θ_v at a given height. The virtual potential temperature is defined as

$$\theta_v = \theta(1 + 0.61q), \tag{1.2}$$

indicating that variations in specific humidity q, independent of temperature, can significantly alter θ_v and thus modify buoyancy.

Buoyancy often plays a dominant role in driving turbulence production within unstable boundary layers under convective conditions. However, mechanical turbulence generated by wind shear can also be significant, especially near the surface or in environments influenced by strong synoptic forcing or storms. Therefore, the spatial structure and variability of moisture play a central role in modulating CBL dynamics, particularly given the challenges traditional modeling approaches face in capturing the influence of buoyancy-driven large-scale motions.

The Monin–Obukhov Similarity Theory (MOST) has long been used to model boundary layer turbulence and is considered a fundamental framework in the field of boundary layer meteorology (Monin and Obukhov 1954). This approach has served as the leading method for turbulence closure, enabling the estimation of turbulent fluxes based on atmospheric stability and mean vertical gradients of the variable of interest.

MOST is widely used in weather and climate models, including the Weather Research and Forecasting (WRF) model and the Community Earth System Model (CESM), to estimate surface fluxes of momentum, heat, and moisture. It is built on the premise that turbulence in the surface layer of the ABL (typically $z/z_i < 0.1$–0.15) can be described using a small set of variables: height above the surface (z), friction velocity

(u_*), and the Obukhov length (L). These form nondimensional similarity parameters that relate turbulent fluxes to stability. MOST's strength lies in its assumptions of horizontal homogeneity and stationarity, making it an elegant and computationally efficient local similarity theory.

While MOST has served as a cornerstone in turbulence modeling (Monin and Obukhov 1954), its inability to represent large-scale turbulence leads to systematic deviations, particularly in convective conditions (Deardorff 1972). As a result, it does not account for the role of coherent structures, known as large-scale motions (LSMs) and very-large-scale motions (VLSMs), where LSMs refer to eddies on the order of the boundary layer depth ($O(z_i)$) and VLSMs are structures approximately ten times that scale ($O(10z_i)$), which modulate small-scale turbulence and fluxes (Adrian 2007; Hutchins & Marusic 2007; Mathis et al. 2009; Ganapathisubramani et al. 2012; Salesky & Anderson 2018). In the CBL, turbulence is non-local and multiscale, and these organized structures can span the entire ABL depth or greater, often dominating vertical transport, processes that MOST does not account for. Consequently, MOST tends to underestimate fluxes and misrepresent variability in such regimes.

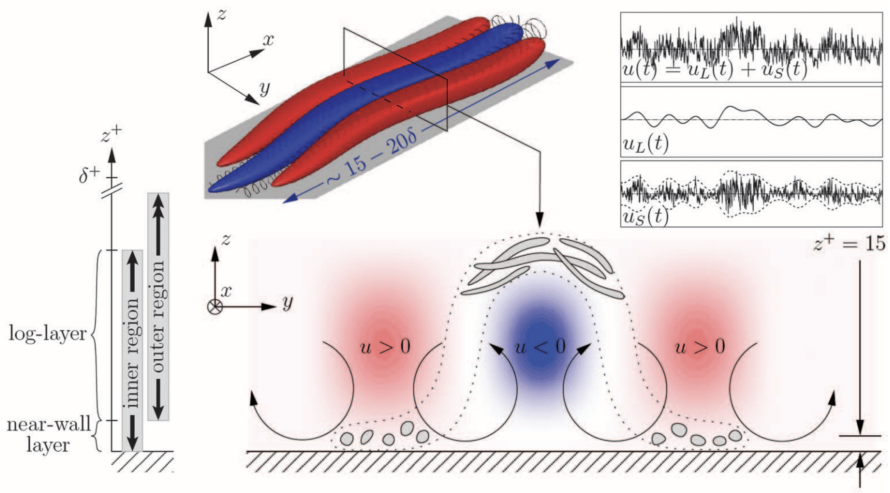

Figure 1.2: Conceptual schematic of wall-bounded turbulence from Marusic et al. (2010). (Left) Layered structure of the turbulent boundary layer, with increasing eddy size from wall to outer region. (Top-middle) Streamwise-aligned VLSMs that can extend over 15 to 20 boundary layer thicknesses. (Top-right) Scale decomposition of velocity fluctuations showing modulation of small-scale activity by large-scale motions. (Bottom) Side view of near-wall coherent structures producing alternating streaks.

Figure 1.2 summarizes key structural and dynamical features of wall-bounded turbulence, as described by Marusic et al. (2010). The left panel shows the classic layered structure of the turbulent boundary layer, with small-scale eddies concentrated near the surface, a logarithmic region in the middle, and increasingly larger motions in the outer region. The top-middle schematic illustrates streamwise-aligned VLSMs, which are long streaks of high and low momentum, capable of extending 15 to 20 times the boundary layer thickness. The top-right panel demonstrates how turbulent velocity fields can be decomposed into large- and small-scale components. Importantly, the small-scale motions are modulated by the large-scale flow, revealing a strong interdependence across scales. This scale interaction is essential for understanding energy cascades and has major implications for turbulence modeling. Finally, the bottom schematic offers a side view of the near-wall region, where coherent vortices produce

alternating high-speed and low-speed streaks through sweep and ejection events. Together, these panels emphasize that wall-bounded turbulence is not purely stochastic but instead exhibits organized, multiscale structure.

Notably, significant differences have been observed in heat versus momentum transport in the CBL, especially under highly convective conditions (large $-z_i/L$). Under unstable conditions, turbulent scalar transport becomes increasingly efficient relative to momentum transport, likely due to the dominance of different coherent structures such as thermal plumes over hairpin vortices (Li & Bou-Zeid 2011). Similarly, Patton et al. (2015) found that large-scale boundary-layer structures can spatially separate momentum and scalar exchange in canopy turbulence, further highlighting this dissimilarity. Furthermore, heat and humidity transport have also been shown to be dissimilar, with entrainment fluxes and scale-dependent decorrelation playing a key role in scalar dissimilarity throughout the CBL (Cancelli et al. 2014), which presents additional complexity for turbulence modeling. Although previous studies have examined momentum transport (e.g., Salesky and Anderson 2018), the effects of LSMs and VLSMs on heat and moisture transport, entrainment, and evaporation remain poorly understood. In particular, the impacts of LSMs on moisture transport have broader implications for the hydrological cycle, including evaporation and cloud development, areas that remain key research gaps. While this study does not directly address these processes, it contributes to understanding the underlying dynamics of moisture transport within the CBL. By investigating these processes using high-resolution observational data from the Southern Great Plains (SGP) Atmospheric Radiation Measurement (ARM) site, this study aims to bridge the gap between observations and numerical modeling, providing deeper insights into scalar transport and entrainment dynamics.

1.3 Research Gap & Questions

While existing studies have extensively analyzed the effects of LSMs and VLSMs on heat and momentum transport in the CBL (e.g. Choi et al. 2004; Patton et al. 2015; Salesky & Anderson 2018), relatively few have explored how LSMs modulate heat and moisture fluxes. This gap in knowledge is compounded by the fact that classical turbulence models, including MOST, fail to account for the influence of these coherent structures on scalar transport within the mixed layer particularly in the presence of large-scale convective motions (Monin & Obukhov, 1954).

Additionally, despite the widespread use of MOST in weather and climate models, its applicability is limited to the atmospheric surface layer. In the convective mixed layer (commonly defined as $0.1 < z/z_i < 0.9$), the relevant scaling framework is mixed-layer similarity theory, which includes z_i as a governing length scale. However, both frameworks often assume scalar similarity and horizontally homogeneous turbulence, assumptions that may not hold under strongly convective conditions. While all scales contribute to the dynamics of turbulence, the role of larger-scale motions, particularly in modulating scalar transport such as moisture and heat, remains poorly understood. These uncertainties raise questions about the ability of current similarity frameworks to adequately represent key processes like evaporation and cloud development within the hydrological cycle and highlight potential gaps in MOST's representation of scalar fluxes within the CBL.

In order to address these gaps, this study will focus on the following key research questions:

1. **How do moisture-related processes influence vertical profiles of turbulent statistics in the CBL?**

This question investigates how vertical profiles of turbulent quantities, specifically $\overline{w'^2}$, $\overline{\theta'^2}$, $\overline{q'^2}$, and $\overline{\theta' q'}$, vary with atmospheric stability, expressed as $-z_i/L$, and surface moisture availability, as characterized by evaporative fraction, E_f. Moisture impacts CBL turbulence primarily through its role in modulating buoyancy, which is a key driver of turbulent kinetic energy (TKE) under convective conditions. Because variations in specific humidity can influence the virtual potential temperature, θ_v, even in the absence of temperature changes, differences in moisture distribution can lead to changes in buoyancy and, consequently, the intensity and vertical structure of turbulence. By relating turbulent variance and covariance profiles to $-z_i/L$ and E_f, this work aims to quantify how surface moisture conditions and boundary layer stability jointly influence scalar transport in the CBL.

2. **Do LSMs in the CBL exhibit similar spectral properties for temperature and humidity?**

   Given the role of LSMs and VLSMs in modulating turbulence, this question investigates whether these structures influence both temperature and humidity fields in a similar manner. If temperature and humidity share similar large-scale structure, this could imply the presence of coherent regions within the CBL where both heat and moisture coincide, enhancing local buoyancy and promoting more vigorous convective activity. In contrast, dissimilar structures may lead to weaker buoyancy and less organized vertical transport. The extent of this similarity likely depends on boundary conditions, including surface and entrainment fluxes, as well as overall atmospheric stability. Addressing this question could lead to more accurate models of scalar transport and improve prediction of weather phenomena such as precipitation and cloud development. While prior work has

explored turbulence spectra for momentum transport, the spectral behavior of temperature and humidity under the influence of LSMs remains underexplored (Deardorff 1972). This study aims to address that gap by examining whether LSMs and VSLMs in the CBL exhibit similar spectral properties for these two scalars.

To investigate these questions, this study analyzes high-resolution observational data collected at the DOE SGP ARM site in Lamont, Oklahoma. The analysis focuses on the summer of 2018, specifically from May 15 to October 15. This period was chosen due to the frequent occurrence of clear-sky, convectively driven boundary layers, as well as consistent and uninterrupted data collection and instrument availability, which allowed for detailed examination of heat and moisture transport processes under varying stability conditions.

Chapter 2

Background & Literature Review

2.1 LSMs, Coherent Structures, and Their Role in Turbulence

A foundational approach to studying turbulence in the ABL is through statistical analysis. Since the late 19th century, researchers have used Reynolds decomposition to separate atmospheric quantities into mean and fluctuating components, for example, decomposing wind speed as $u = \overline{u} + u'$ and temperature as $\theta = \overline{\theta} + \theta'$. This framework allows turbulent flows to be described in terms of statistical moments such as means ($\overline{u}$, $\overline{\theta}$), variances ($\overline{u'^2}$, $\overline{w'^2}$), and covariances ($\overline{w'\theta'}$, $\overline{u'w'}$), which serve as indicators for the intensity and transport properties of turbulence.

While this statistical perspective remains fundamental, it was recognized in the 1970s and 1980s that turbulence also exhibits spatial and temporal organization (Brown and Thomas 1977; Head & Bandyopadhyay 1981). Starting in the late 1800s, turbulence was thought to be purely random, characterized as a chaotic, stochastic mess of swirling motions that defied prediction. As measurement techniques and computational tools improved, a very different picture began to emerge. Rather than being entirely random, it was seen that turbulent flows contain coherent structures, recurrent patterns, or motions that contribute significantly to transport processes (Corino

& Brodkey 1969; Adrian et al. 2000). In the CBL, such structures often take the form of LSMs and VLSMs.

A key moment in this shift came with the 1968 Kansas Experiment, which was one of the first major field campaigns to measure turbulence in the atmospheric surface layer with high spatial and temporal resolution. This field campaign is considered to be an important milestone in the history of ABL research. This project supplied data which provided strong empirical support for MOST, showing that turbulence could be scaled, modeled, and even predicted based on well-defined physical parameters (Businger et al. 1971; Kaimal et al. 1972; Kaimal & Wyngaard 1990). After this campaign, turbulence was not just seen as disorder, it became something we could quantify, model and understand through coherent structures, scaling laws, and theory-informed measurements.

Understanding turbulence in the ABL requires recognizing the influence of coherent structures that extend across large vertical scales. LSMs and VLSMs are fundamental to the organization and dynamics of turbulent flows in the ABL. These structures, which span the entire depth of the ABL or more, on the order of $O(z_i)$ and $O(10z_i)$, exert significant control over small-scale turbulence on the vertical transport of momentum, heat, and moisture.

Laboratory and theoretical studies paved the way for extending these ideas to atmospheric flows. Early work by Brown and Thomas (1977) and Head and Bandyopadhyay (1981) in wall-bounded turbulence identified elongated low-momentum structures, showing that they extend across multiple boundary layer depths. Laboratory studies, including Kim and Adrian (1999), further demonstrated that LSMs in neutrally stratified, wall-bounded flows (e.g. channels and pipes) play a crucial role in momentum exchange. These discoveries challenged the traditional view of the boundary layer as a random field of eddies, instead revealing a highly organized structure with coherent

features that modulate small-scale turbulence. While initially observed in laboratory flows, these structures have clear analogs in boundary layers. Their influence on scalar and momentum transport is increasingly recognized, particular under convective conditions. Recent observational studies using high-resolution lidar, such as Turner et al. (2014), have demonstrated that turbulence in water vapor profiles also exhibit coherent vertical structure in the CBL, underscoring the need to consider humidity as an active component of boundary-layer dynamics.

In CBLs, LSMs manifest as coherent updrafts and downdrafts, often organized into convective rolls or vortices, which drive vertical mixing. These organized motions dominate the transport of momentum and scalar quantities, such as heat and moisture. Adrian et al. (2000) and Tomkins and Adrian (2003) showed that such structures, including hairpin vortex packets, play a significant role in turbulent bursts and enhance mixing.

Beyond their qualitative description, the spatial and temporal characteristics of LSMs relate directly to boundary layer conditions. Although LSMs and VLSMs were initially identified in neutrally stratified wall-bounded flows (Mathis et al. 2009; Ganapathisubramani et al. 2012) as low-momentum streaks in the streamwise velocity component ($u' < 0$), in convective conditions they are also evident in the vertical velocity field. In the CBL, regions of positive vertical velocity fluctuations ($w' > 0$) often align with negative streamwise fluctuations ($u' < 0$), making vertical velocity a useful indicator of these structures. Such structures are not just incidental features, but are integral to the vertical organization of turbulent energy and scalar transport. For instance, the spacing and coherence of convective rolls have been observed to depend on surface heat flux and boundary layer depth, suggesting that their influence scales with key physical drivers of CBL development.

Despite this growing understanding of the momentum effects of LSMs, their role in scalar transport remains an open question. Although momentum transport has been extensively studied, including through parameterizations developed by Louis (1979) and Beljaars (1995), the modulation of scalar quantities like temperature and humidity by LSMs remains poorly understood.

Some recent studies, though primarily focused on canonical flows, provide insight into how such structures might modulate scalar fluxes. Adrian (2007) argued that organized structures like hairpin vortices strongly affect scalar transport, with vertical updrafts and downdrafts enhancing or suppressing fluxes depending on how they interact with scalar gradients. Guala et al. (2006) and Hutchins and Marusic (2007), though focused on canonical flows like turbulent pipe and channel flow, found that LSMs and VLSMs modulate TKE and Reynolds stresses across multiple scales. While their work concentrated on momentum transport, the multiscale organization they identified suggests that similar structural influences may extend to scalar transport in the ABL.

2.2 Mixed-Layer Similarity Theory

Having established the significance of large-scale coherent structures in turbulent transport within the CBL, it is essential to examine how classical turbulence theories incorporate or neglect these influences. MOST, developed by Monin and Obukhov (1954), provides a foundational framework for modeling turbulence in the surface layer of the ABL. It predicts turbulent fluxes using a dimensionless stability parameter $(-z/L)$, where L is the Obukhov length. MOST assumes horizontally homogeneous, stationary turbulence and incorporates only the distance from the surface (z) as the relevant length scale. It is widely used in both weather and climate models.

Despite its utility, MOST has well-known limitations, especially under strongly convective conditions (Cancelli et al. 2012; Cancelli et al. 2014). Because it is based on dimensional analysis that includes only local scales (e.g. z, u_*, and L), it inherently neglects non-local influences. In unstable boundary layers, this leads to the exclusion of large-scale structures such as LSMs and VLSMs, which play a dominant role in turbulent transport. As Deardorff (1972) noted, the absence of such non-local dynamics introduces systematic biases, particularly in modeling vertical fluxes of heat and moisture in the CBL.

Building on MOST, which is formally applicable to the atmospheric surface layer (typically for $z/z_i < 0.1$ to 0.15), classical mixed-layer similarity theory attempts to extend scaling relationships to the interior of the CBL, usually defined over $0.1 < z/z_i < 0.9$. This framework assumes that turbulent statistics can be scaled using a limited set of governing variables: the height z, boundary layer depth z_i, friction velocity u_*, the buoyancy parameter g/Θ_0, and the surface heat flux $\overline{w'\theta'}$. When normalized by the appropriate mixed-layer scales, z_i for length, the convective velocity scale $w_* = (\frac{g}{\Theta_0}\overline{w'\theta'}z_i)^{1/3}$ for velocity, $\theta_* = \overline{w'\theta'}/w_*$ for temperature, and $q_* = \overline{w'q'}/w_*$ for humidity, dimensionless turbulence statistics are predicted to be functions of normalized height z/z_i and global stability $-z_i/L$.

While powerful, this framework has important limitations. It presumes horizontally homogeneous, stationary conditions and treats turbulence as a local process governed entirely by vertical gradients and surface forcing. Such assumptions overlook the multiscale, coherent nature of turbulence, particularly in convective regimes where large structures span a significant fraction of the boundary layer depth. Consequently, this framework cannot fully capture the influence of LSMs and VLSMs on turbulent transport.

Further complicating the picture, classical similarity theory assumes that scalar quantities such as temperature and humidity behave similarly in turbulent transport. In reality, the diffusivity of heat exceeds that of water vapor, and humidity is influenced by surface evaporation, latent heat release, and entrainment from the free atmosphere. These factors result in scalar transport characteristics that differ from those of temperature, yet these differences are not captured by classical similarity theory. Turner et al. (2014) provides observational evidence from Raman lidar that water vapor behaves differently from temperature in terms of vertical turbulent structure and spectral content. Their results showed that vertical profiles of water vapor variance deviate from similarity predictions, particularly under varying surface flux conditions, reinforcing the breakdown of scalar similarity in the CBL.

Wyngaard et al. (1978) provides one of the earliest comprehensive analyses of the temperature-humidity covariance budget in the CBL. Their study, based on data from the Air Mass Transformation Experiment (AMTEX) and other campaigns, such as the 1968 Kansas Experiment (discussed in Section 2.1), identified that in the near-neutral surface layer, the production of temperature and humidity fluctuations is approximately balanced by their molecular dissipation, while in the mixed layer, turbulent transport processes become increasingly significant.

Findings by Cancelli et al. (2012) offer additional insight into this phenomenon by demonstrating that imbalances in scalar variance and covariance budgets are key contributors to the breakdown of scalar similarity. Using observational data collected over a tropical lake in Brazil, they found that scalar similarity between temperature and water vapor deteriorates under strong surface forcing, primarily due to disruption of the classical equilibrium between gradient production and molecular dissipation. Their analysis highlighted the significant role of large third-order transport terms, and potentially nonstationary processes, in affecting this balance. They introduced

dimensionless scalar flux numbers and a robust bulk indicator of scalar flux similarity, applicable in both physical and spectral domains, reinforcing that scalar dissimilarity arises from fundamental physical mechanisms rather than measurement uncertainty or surface variability.

Complementing these scalar-focused studies, empirical studies from engineering and fluid dynamics research underscore these theoretical limitations by emphasizing the role of large-scale structures in turbulence modulation. For example, Guala et al. (2006) demonstrated that LSMs influence the distribution of TKE and Reynolds stress through multiscale interactions in canonical flows. Similarly, Hutchins and Marusic (2007) observed that very-large-scale "superstructures" impact near-surface turbulence, suggesting a top-down modulation of turbulence. While these studies focus primarily on momentum transport in wall-bounded turbulent flows such as pipes and channels, their findings imply that large-scale coherent structures in the ABL may exert comparable multiscale control, potentially extending to scalar transport under convective conditions.

2.3 Parameter Framework for the Moist CBL

The previous section outlined how classical similarity theories, while foundational, fail to account for non-local effects and the multiscale structure of turbulence in the CBL. To address these shortcomings, especially in the context of scalar transport, an expanded framework is needed. This framework must incorporate both surface and entrainment processes and account for the differing behavior of various scalars such as temperature and humidity.

Classical mixed-layer similarity relies primarily on the dimensionless variables z/z_i and $-z_i/L$. However, when latent heat flux dominates, additional parameters are needed to describe the turbulent structure and variability of moisture.

One such parameter is the evaporative fraction (E_f), defined as:

$$E_f = \frac{LE}{LE + H} = \frac{1}{1 + B} \tag{2.1}$$

where $LE = \rho L_v \overline{w'q'}_0$ is the latent heat flux and $H = \rho c_p \overline{w'\theta'}_0$ is the sensible heat flux, with ρ as air density, L_v as the latent heat of vaporization, and c_p as the specific heat at constant pressure. The evaporative fraction captures the partitioning of available energy at the surface. It is inversely related to the Bowen ratio (B), defined as $B = H/LE$. When $E_f = 0$, there is no latent heat flux and all available energy goes into sensible heating. Conversely, when $E_f = 1$, there is only latent heat flux and no sensible heating. Higher values of E_f correspond to more energy being allocated to evaporation, resulting in moister boundary layers with stronger vertical humidity gradients. In contrast, low values of E_f indicate drier surfaces and greater heating of the near-surface air. This partitioning modulates the strength and structure of convective updrafts and, consequently, the vertical transport of humidity.

Another critical parameter is the humidity entrainment flux ratio (ϕ_{wq}), which characterizes the relative influence of surface versus entrainment fluxes of moisture. It is defined as:

$$\phi_{wq} = \arctan\left(\frac{\overline{w'q'}_0}{\overline{w'q'}_{z_i}}\right), \tag{2.2}$$

where $\overline{w'q'}_0$ is the surface kinematic humidity flux, and $\overline{w'q'}_{z_i}$ is the entrainment flux at the inversion. The arctangent is used so that ϕ_{wq} is a bounded metric, with values constrained between $-90°$ and $+90°$. A negative ϕ_{wq} indicates net moistening of the

boundary layer from above, while a positive value implies drying due to entrainment of drier air from the free atmosphere. This parameter serves as a diagnostic of the moisture budget and the vertical structure of humidity variance in the CBL.

While this study primarily focuses on the influence of E_f and does not directly analyze ϕ_{wq}, understanding turbulent mixing and entrainment into the ABL remains essential for interpreting moisture transport dynamics.

These additional parameters allow for a more complete description of scalar variability in the CBL, helping to address the limitations of classical similarity theory. Future studies can use this expanded framework to refine parameterizations and improve predictions of scalar transport, especially under strongly convective conditions. Turner et al. (2014) also highlighted the importance of considering both surface flux partitioning and entrainment when interpreting moisture variability in the CBL. Their results, derived from Raman lidar data at the SGP site, parallel the objectives of this study and validate the use of evaporative fraction and normalized height in characterizing humidity structure.

Together, insights from coherent structures, classical and extended similarity theory, and scalar transport dynamics provide the theoretical foundation for this thesis. The next chapter outlines the methodology used to evaluate vertical turbulent fluxes and scalar variability within the CBL using high-resolution observations.

Chapter 3

Data & Methodology

3.1 Data Sources

The SGP site is an atmospheric observatory and is the primary research site of the U.S. Department of Energy's ARM program. Established in 1992, the SGP site spans approximately 9,000 square miles across north-central Oklahoma and southern Kansas (Figure 3.1). Its Central Facility, located on a 160-acre plot in Lamont, Oklahoma (Figure 3.2), serves as the core hub for continuous atmospheric observations (ARM | Southern Great Plains).

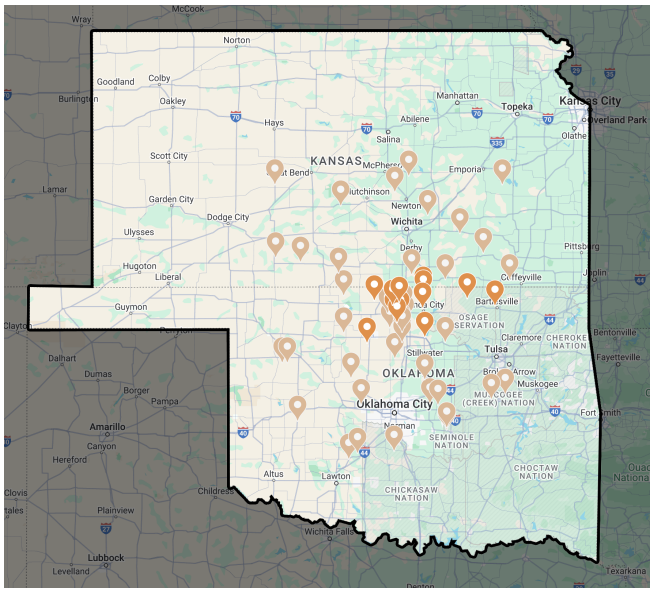

Figure 3.1: Map highlighting Oklahoma and Kansas with orange markers indicating locations of all SGP facilities.



Figure 3.2: Map of Oklahoma with red star indicating location of the SGP ARM site in Lamont, Oklahoma.

The SGP site is widely recognized as the world's leading ground-based facility for studying atmospheric processes. It hosts over 50 instrument platforms, including a suite of radiometers, radars, and lidars; surface meteorological instruments; aerosol and cloud measurement systems; and radiosonde launch capabilities (ARM | Southern Great Plains). These instruments provide high-resolution observations of the thermodynamic, radiative, and turbulent structure of the atmosphere.

All data collected at the SGP site are transmitted to the ARM Data Center and are freely available to the scientific community through the ARM Data Discovery platform (https://adc.arm.gov). This extensively and publicly accessible archive enables long-term studies of boundary layer processes, cloud and aerosol interactions, radiation budgets, and land-atmosphere coupling.

This study utilizes a subset of high-resolution observations collected at the SGP Central Facility during the summer of 2018. The following section outlines the specific instruments and data products used in this study, along with the criteria applied to identify and filter CBL cases for analysis.

To identify cases for this project, each hour within the initial time frame was examined and filtered based on specific criteria. We gathered solar radiation, cloud cover,

ABL depth (z_i), Doppler lidar, Raman lidar, and eddy correlation (ECOR) data from the DOE ARM website to calculate additional ABL measurements. Using the ARM Data Discovery platform, each data type was streamed directly into the code and downloaded directly into the computing cluster for the dates analyzed. To determine which cases to examine further, we calculated the Obukhov length (L) and the convective velocity scale (w_*). These diagnostics were used to identify daytime periods characterized by unstable, convectively-driven boundary layers.

For documentation purposes, each ARM dataset is associated with a unique file name that encodes the site, instrument type, facility code, and data level. For example, the Total Sky Imager (TSI) data used for solar radiation and cloud cover analysis is identified by the stream name *sgptsiskycoverC1.b1*. A complete list of the instruments used in this study, along with their corresponding data stream names and temporal/spatial resolution is provided in Table 3.1.

Data Type	**ARM Data Name**	**Temporal Resolution**	**Spatial Resolution**	**Variables Used**
Doppler Lidar	sgpdlfpt	3 seconds	30 meters	Vertical velocity $w(z)$
Doppler Lidar Wind VAP	sgpdlprofwind4news	15 minutes	26 meters	Horizontal wind profile $U_h(z)$
ECOR	sgp30ecor	30 minutes	N/A	Surface fluxes
Raman Lidar	sgprlprofmr2news	10 seconds	60 meters	Temperature $\theta(z)$, Humidity $q(z)$
Sawyer-Li (z_i)	sgpblhtmpl1sawyerli	30 minutes	30 meters	ABL height z_i
Total Sky Imager	sgptsiskyclover	30 seconds	N/A	Total sky cover

Table 3.1: Summary of Southern Great Plains (SGP) Atmospheric Radiation Measurement (ARM) observational datasets used in this study, including data type, ARM product name, temporal and spatial resolutions, and the primary variables used from each product.

3.2 Instrumentation & Measurements

3.2.1 Total Sky Imager (TSI)

The TSI used in this study is the Model 880, manufactured by Yankee Environmental Systems (YES), Inc. The TSI 880 is an advanced commercialized version of the Hemispheric Sky Imager prototype developed by Long et al. (1998). It was first deployed at the Blackwell Tonkawa Airport during the 2000 ARM Cloud Intensive Operational Period (IOP) and has since been used extensively at the SGP Central Facility (Morris 2005).

The TSI uses a rotating, heated hemispheric mirror and collects data with a temporal resolution of 30 seconds. A shadowband on the mirror blocks direct solar radiation, allowing a solid-state charge-coupled device (CCD) imaging camera positioned above the mirror to capture clear-sky and clouded environments. An image processing algorithm masks obstructions (e.g., the shadowband, arm, and imager housing) and classifies pixels as clear sky, thin clouds, or opaque clouds (Morris 2005). These classifications are archived as fractional sky cover and used in this study to filter for clear-sky cases.

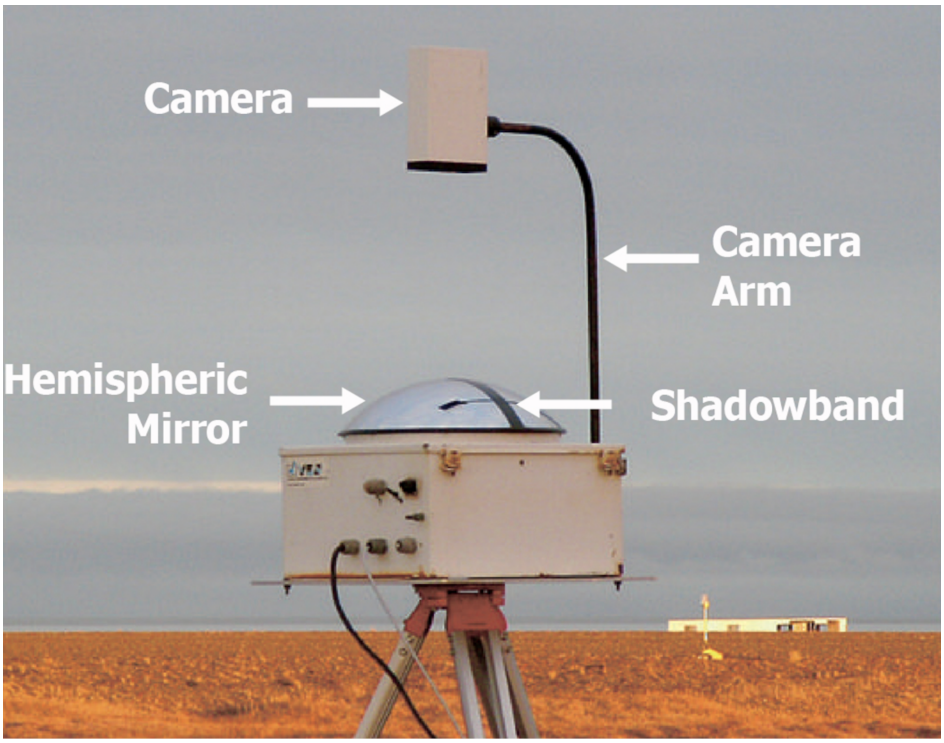

Figure 3.3: Labeled image of the Total Sky Imager. Image provided by ARM TSI Handbook (Morris 2005).

3.2.2 Doppler Lidar (DL)

The Doppler lidar (DL) used is the Stream Line Pro model from Halo Photonics, an active remote sensing instrument that emits pulses of laser energy vertically into the atmosphere and measures the Doppler shift of aerosol backscatter to determine atmospheric motion. The DL provides range- and time-resolved measurements of vertical velocity, signal-to-noise ratio, and attenuated backscatter (Newsom & Krishnamurthy 2022). It emits pulses of electromagnetic energy in the visible range into the atmosphere, providing measurements with a temporal resolution of 3 seconds and a vertical resolution of 30 meters. When pointed vertically, the DL measures the vertical component of radial velocity, which is defined as positive for motion away from the lidar and negative for motion toward the lidar.

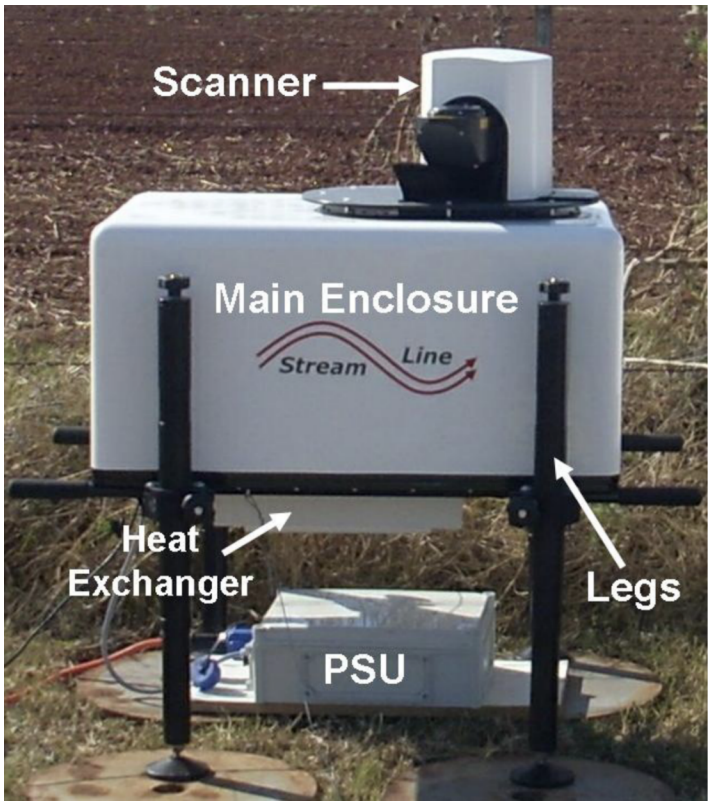

Figure 3.4: Labeled image of Doppler Lidar. Image provided by ARM DL Handbook (Newsom & Krishnamurthy 2022).

To estimate horizontal wind profiles, this study utilizes the Doppler Lidar Wind Profile Value-Added Product (VAP), designated as *sgpdlprofwind4newsC1.c1.* Accurate, high-resolution wind measurements are essential for understanding boundary layer turbulence, and the VAP provides vertically resolved horizontal wind (u) data within the ABL. For each case, the mean horizontal wind component at each normalized height (z/z_i) was computed (e.g. Figure 3.5). This product is derived from scanning coherent Doppler lidars, which retrieve wind velocities by measuring laser backscatter from atmospheric aerosols (ARM 2014). The VAP offers a temporal resolution of 15 minutes and a vertical resolution of 26 meters, making it well suited for detailed analysis of wind shear. In this study, the mean horizontal wind profiles extracted from the VAP were converted to normalized height coordinates (z/z_i) and used as velocity

inputs to calculate characteristic wavelengths, which were then applied to generate spectrograms for vertical velocity, temperature, and humidity, as described later in the results section.

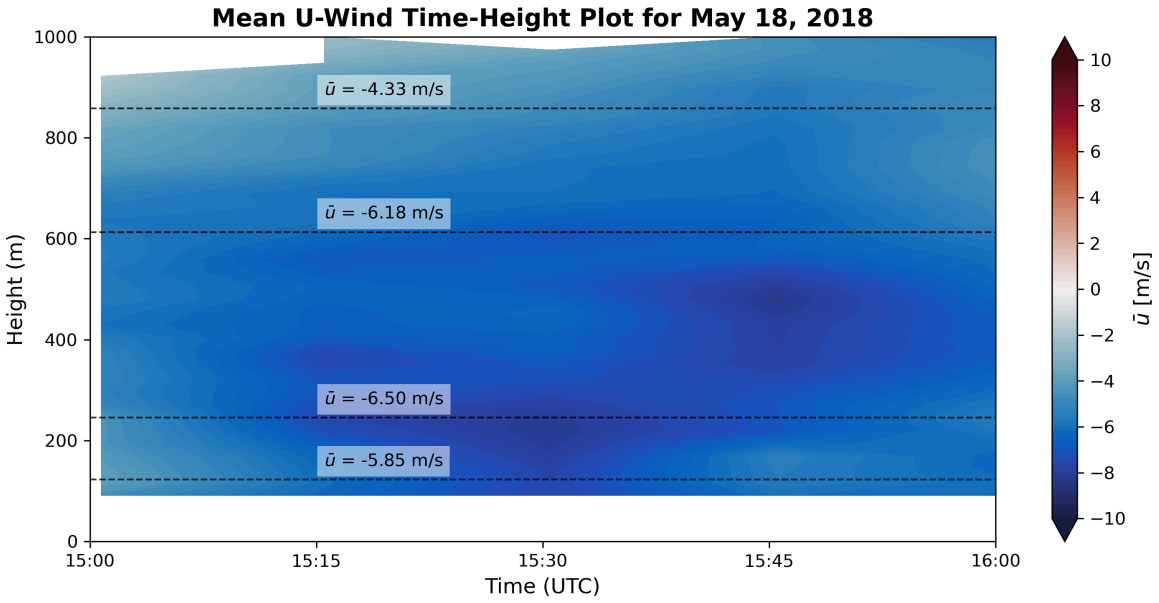

Figure 3.5: Time–height cross-section of mean zonal wind ($\bar{u}$) from Doppler lidar measurements on May 18, 2018, between 15:00–16:00 UTC. The color shading indicates the magnitude of $\bar{u}$ (m/s), with negative values representing westerly flow. Dashed black lines mark selected altitudes within the boundary layer where zonal winds are averaged for further analysis. Mean values of $\bar{u}$ at these levels are annotated directly on the plot.

3.2.3 Eddy Correlation (ECOR) System

Eddy covariance data was collected at the Lamont (E14) site using instruments developed by Gill Instruments and LI-COR Biosciences, identified as *sgp30ecorE14.b1*. The system includes a 3D sonic anemometer for high-frequency wind measurements, and an infrared gas analyzer (IRGA) for measuring latent heat flux, carbon dioxide (CO_2), and methane (CH_4) concentrations. The data has a temporal resolution of 30 minutes (Cook 2018).

These instruments provide direct measurements of surface turbulent fluxes, which are calculated using covariance relationships between vertical wind fluctuations and scalar fluctuations. Key quantities derived from the ECOR system include sensible heat flux (H), latent heat flux (LE), friction velocity (u_*), convective velocity scale (w_*), Bowen ratio (B), and evaporative fraction (E_f) (Cook 2018). These quantities are fundamental for characterizing surface energy partitioning and turbulent transport processes in the CBL.

- **Sensible heat flux (H):**

$$H = \rho c_p \overline{w'\theta'}_0 \tag{3.1}$$

  where ρ is air density, c_p is the specific heat at constant pressure, w' is the vertical velocity fluctuation, and θ' is the potential temperature fluctuation.

- **Latent heat flux (LE):**

$$LE = \rho L_v \overline{w'q'}_0 \tag{3.2}$$

  where L_v is the latent heat of vaporization and q' is the specific humidity fluctuation.

- **Friction velocity (u_*):**

$$u_* = \left(\overline{u'w'}^2 + \overline{v'w'}^2\right)^{1/4} \tag{3.3}$$

  where u' and v' are the horizontal wind fluctuations in the x and y directions.

- **Convective velocity scale (w_*):**

$$w_* = \left(\frac{g z_i \overline{w'\theta'}}{\theta_0}\right)^{1/3} \tag{3.4}$$

where g is gravitational acceleration, θ_0 is a reference potential temperature, and z_i is the boundary layer depth.

- **Bowen ratio (B):**

$$B = \frac{H}{LE} \tag{3.5}$$

representing the ratio of sensible to latent heat flux.

- **Evaporative fraction (E_f):**

$$E_f = \frac{LE}{LE + H} \tag{3.6}$$

which indicates the fraction of available energy used for evaporation.

3.2.4 Atmospheric Boundary Layer Depth (z_i)

ABL height (z_i) was retrieved using the Sawyer-Li method, which estimates boundary layer depth from micropulse lidar (MPL) backscatter profiles (Sawyer & Li 2013). This method involves three key steps. First, a wavelet covariance transform using a Haar wavelet identifies the strongest vertical drop in aerosol backscatter, providing an initial estimate of the ABL height and the entrainment zone depth. Second, a simulated annealing optimization refines this estimate by fitting an idealized curve to the backscatter profile, helping avoid local minima that often hinder standard curve-fitting techniques (Eqn. 3.7) . Finally, a 25-minute running mean is applied to the time series to smooth out short-term fluctuations caused by noise or variability in the lidar signal (Sawyer & Li 2013). Physically, this approach exploits the sharp gradient in aerosol concentration at the top of the ABL, where well-mixed, particle-rich air gives way to cleaner free-tropospheric air. The processed product was downloaded directly from the ARM Data Discovery platform, with a temporal resolution of 30 minutes and

a vertical resolution of 30 meters. For each case, z_i was averaged over the hour to provide a single representative boundary layer depth as seen in Figure 3.6.

$$B(z) = \frac{B_m + B_u}{2} - \frac{B_m - B_u}{2} \operatorname{erf}\left(\frac{z + z_m}{s}\right) \tag{3.7}$$

where B_m is the mixed layer backscatter, B_u is the free troposphere backscatter, z_m is the ABL depth, and s is the depth of the idealized curve between B_m and B_u.

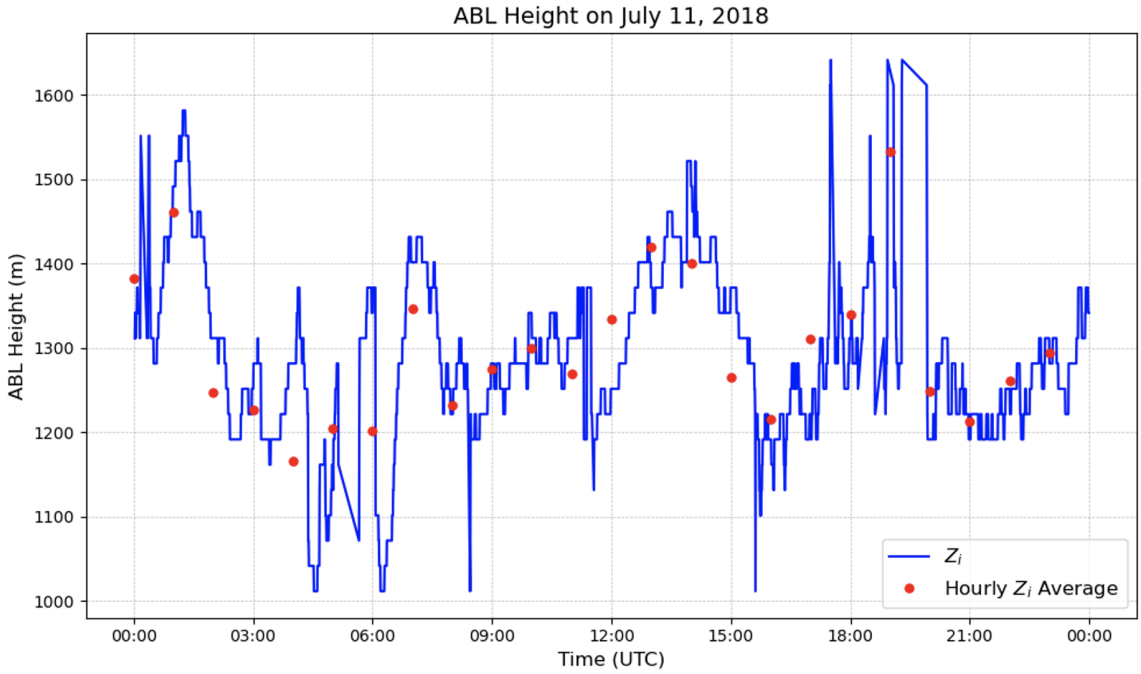

Figure 3.6: Change of ABL depth over 24 hours. The blue line indicates raw z_i data and red dots show calculated 1-hour averages of z_i.

3.2.5 Raman Lidar (RL)

The Raman Lidar (RL) at the SGP Central Facility is a semi-automatic, ground-based laser remote-sensing instrument designed to provide height- and time-resolved profiles of key atmospheric variables. These include water vapor mixing ratio, temperature, aerosol backscatter, extinction, and linear depolarization ratio (Newsom et al. 2022).

Measurements span altitudes from approximately 200 meters to over 10 kilometers above ground level, enabling detailed observation of vertical structure in the boundary layer and free atmosphere above.

For this project, data were obtained from the *sgprlprofmr2newsC1.c0* datastream, which contains quality-controlled Raman lidar profiles. The RL provides observations with a temporal resolution of 10 seconds and a vertical resolution of 60 meters, making it well suited for resolving fast-evolving processes such as scalar transport, entrainment, and humidity variability in the CBL.

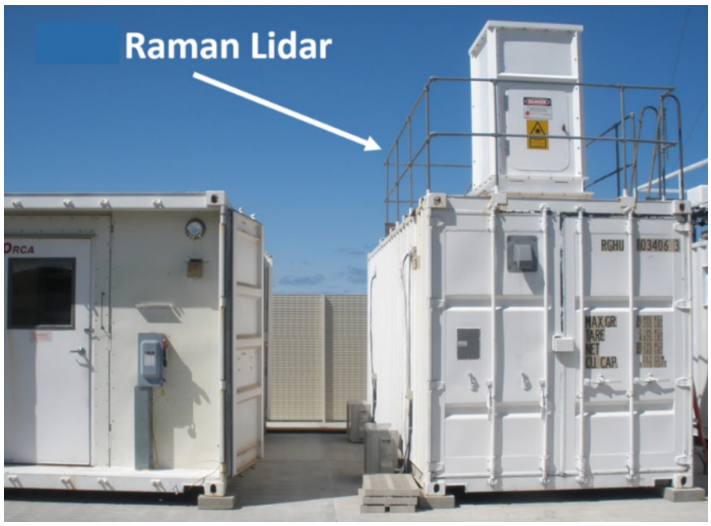

Figure 3.7: Labeled image of Raman Lidar. Image provided by ARM RL Handbook (Newsom et al. 2022).

3.3 Data Preprocessing & Selection Criteria

The data used in this study were collected from May 15, 2018, to October 15, 2018, at the SGP ARM site. To ensure the accuracy and relevance of the analysis, a series of preprocessing and selection steps were applied to the dataset. These steps are outlined below. First, the data were segmented into hourly intervals to ensure uniform sampling across all cases. This hourly segmentation allowed for consistent analysis

of CBL dynamics over time, which provided a stable temporal framework for cross-instrument comparisons and enabled for better integration of the data.

1. **Timeframe:** The timeframe from May 15 to October 15, 2018 was selected to capture the peak summer season, when CBL activity is typically strongest. This period also offered an abundance of clear-sky conditions and reliable, continuous data coverage from the SGP instrumentation, providing an ideal window for examining heat and moisture transport across a range of atmospheric stability regimes.

2. **Cloud Cover and Radiation Daytime:** Only hours with less than or equal to 5% cloud cover during the daytime were included, resulting in 209 cases. This filter ensures that the data represent clear-sky conditions when the CBL is active, which are essential for analyzing the turbulent fluxes within the ABL.

3. **Obukhov Length (L):** Unstable boundary layer conditions were identified by calculating the Obukhov Length using the following equation:

$$L = -\frac{u_*^3 \theta_0}{\kappa g Q_0} \tag{3.8}$$

where u_* is the friction velocity, θ_0 is the reference potential temperature, $\kappa = 0.4$ is the von Kármán constant, g is gravitational acceleration, and Q_0 is the kinematic surface heat flux, defined as:

$$Q_0 = \frac{H}{\rho c_p} = \overline{w'\theta'}_0 \tag{3.9}$$

Physically, the Obukhov Length represents the height at which buoyancy begins to dominate over mechanical shear in generating turbulence. When L is negative,

it indicates an unstable CBL, where surface heating enhances vertical mixing through buoyancy. The magnitude of $-z_i/L$, where z_i is the ABL depth, serves as a measure of instability, with larger values indicating more strongly convective conditions (Stull 1988; Wyngaard 2010). Only cases with negative values of L were selected, yielding 136 cases representing periods when convective turbulence is expected to dominate the boundary layer. Figure 3.8 illustrates the distribution of L for the final cases.

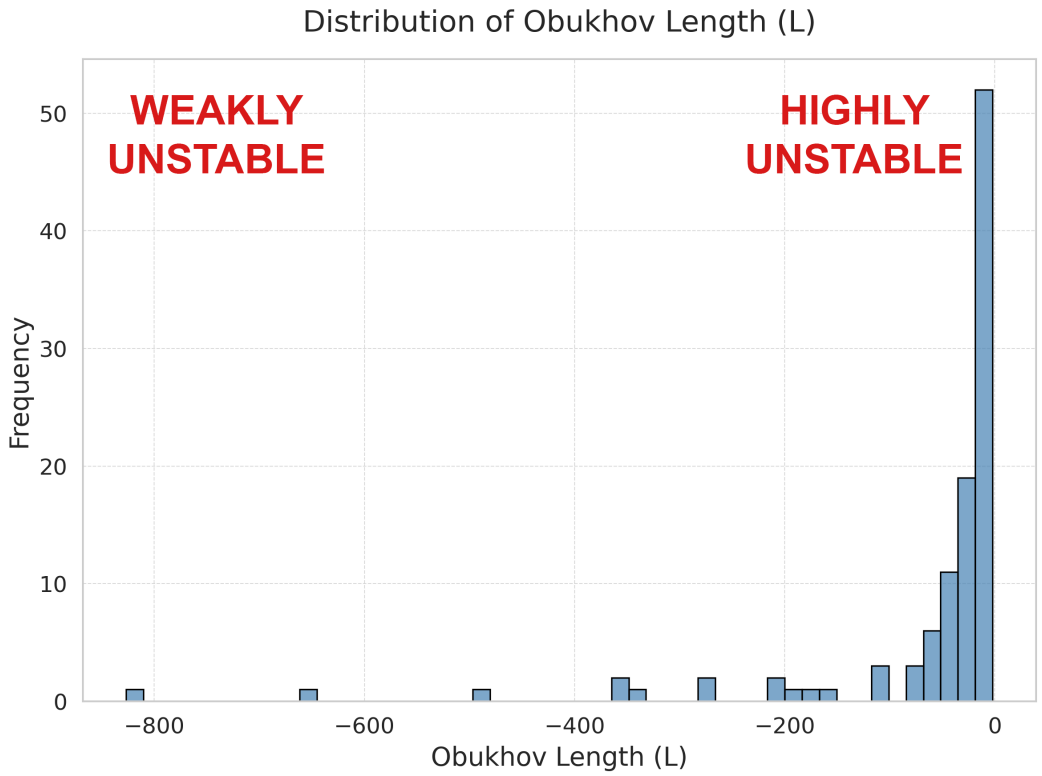

Figure 3.8: Histogram of Obukhov Length (L) for the final 107 cases.

4. **Boundary Layer Depth (z_i):** Some hours of data were missing boundary layer depth measurements, and these cases were excluded from the analysis. After this step, 130 cases remained, corresponding to times when z_i was measured and reliable. Figure 3.9 illustrates the distribution of z_i for the final cases.

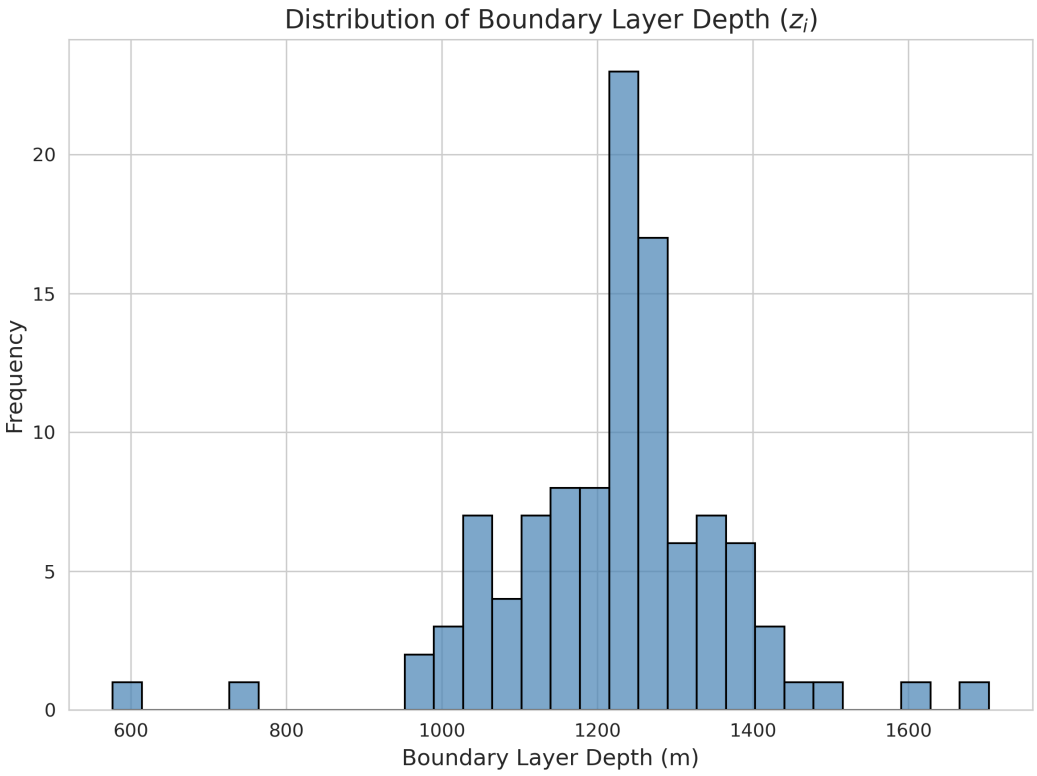

Figure 3.9: Histogram of boundary layer depth (z_i) for the final 107 cases after filtering.

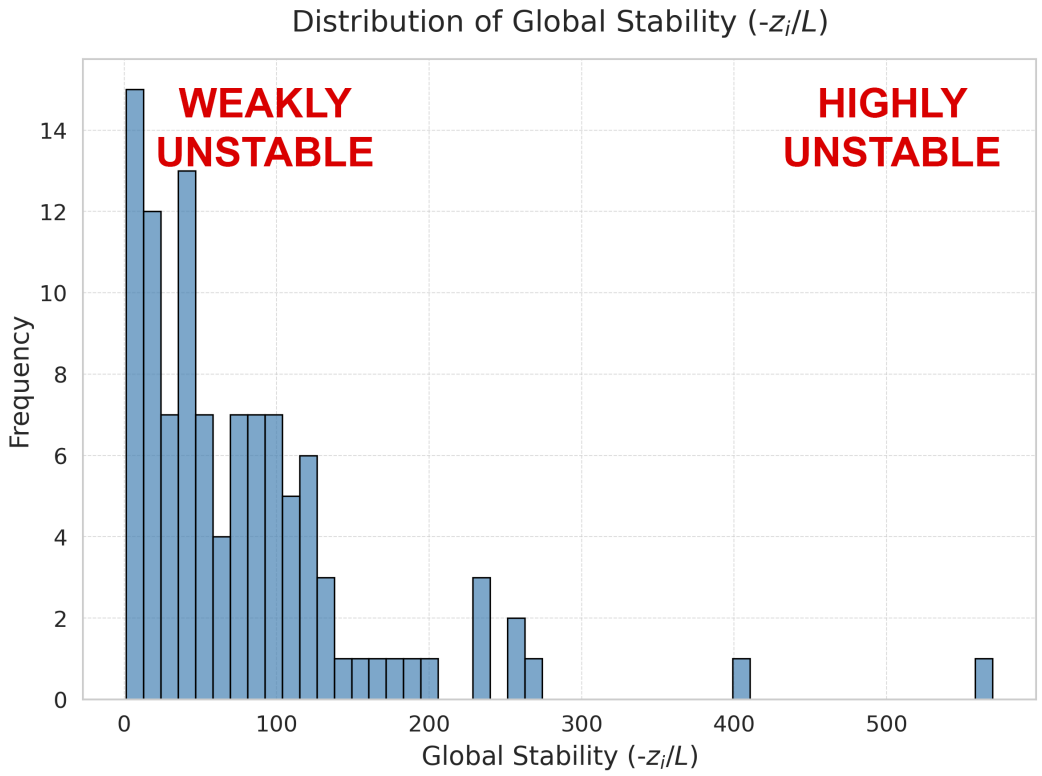

Figure 3.10: Histogram of global stability parameter $(-z_i/L)$ for the final 107 cases.

5. **Convective Velocity Scale (w_*):** Cases with negative values for the convective velocity scale were excluded, as they are not consistent with the expected positive buoyancy flux in unstable boundary layer conditions. This selection resulted in 124 cases with positive values of w_*.

6. **Raman Lidar Data:** Certain hours of RL data were missing, so these cases were also excluded. After this final filtering step, 107 cases remained, ensuring the presence of complete lidar data for analysis.

The final dataset consisted of 107 cases that met all of the above criteria, providing a robust sample for investigating the dynamics of the CBL and turbulent fluxes during the summer of 2018.

3.4 Analysis Methods

Atmospheric stability is a key driver of turbulent transport processes in the CBL. A fundamental measure of this stability is the dimensionless global stability parameter, $-z_i/L$, which quantifies the relative contributions of shear and buoyancy to turbulence generation. When $-z_i/L$ is small (weak instability), turbulence is predominantly shear-driven, often favoring horizontal roll structures. As instability increases (i.e., $-z_i/L$ rises), buoyancy becomes the dominant source of turbulence, leading to a transition from roll-like to more cellular convection. During this shift, convective roll structures begin to break down, giving way to enhanced vertical transport of heat and moisture by buoyancy-driven turbulence (Salesky et al., 2017).

For this observational analysis, boundary-layer conditions were classified into three regimes based on the value of $-z_i/L$: weakly unstable ($0 \leq -z_i/L < 10$), moderately unstable ($10 \leq -z_i/L < 50$), and highly unstable ($-z_i/L > 50$). These classification distributions can be seen in Figure 3.11 and Figure 3.12. Prior research (e.g., Salesky et al., 2017) suggests that the most rapid transitions in convective structure and turbulent fluxes occur within this range. Using this classification, high-resolution observational data from DL, RL, and ECOR instruments were analyzed to examine how convective organization influences heat and moisture transport, entrainment flux ratios, and turbulent mixing efficiency across different stability regimes.

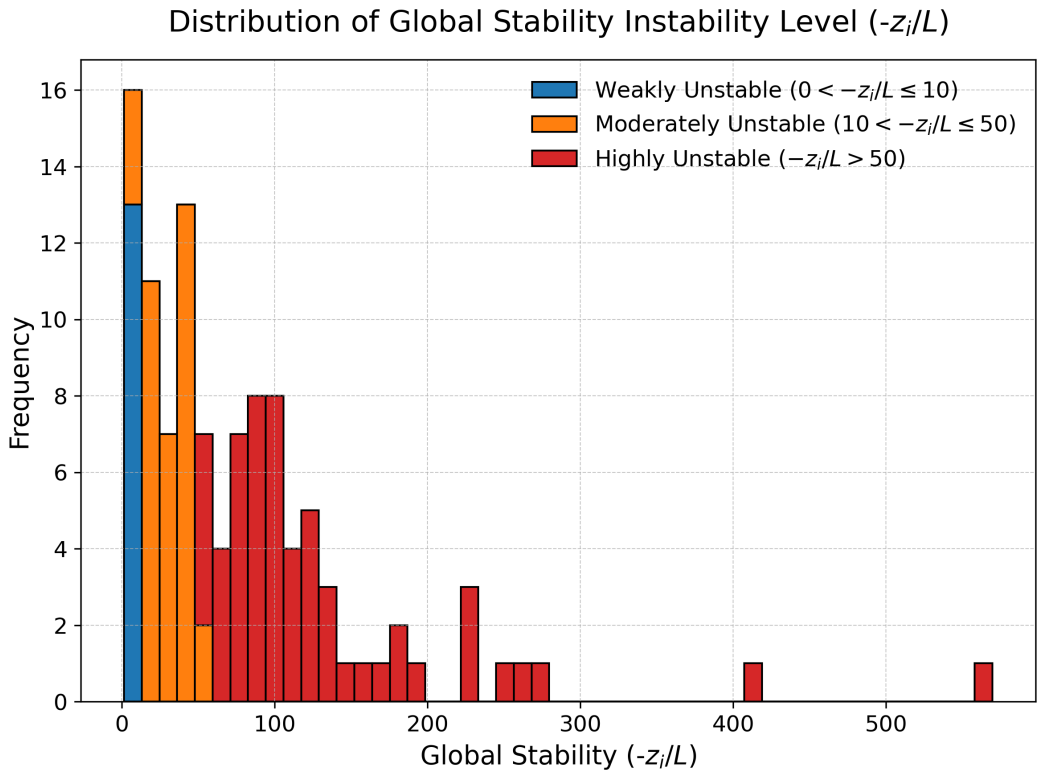

Figure 3.11: Distribution of the global stability parameter $(-z_i/L)$ across observed cases. The dataset is categorized into three regimes: weakly unstable ($0 < -z_i/L \leq 10$, blue), moderately unstable ($10 < -z_i/L \leq 50$, orange), and highly unstable ($-z_i/L > 50$, red). The histogram illustrates the frequency of occurrences within each regime, highlighting the transition from shear- to buoyancy-dominated turbulence.

To further examine the relationship between turbulence dynamics and atmospheric stability, the Obukhov length (L) is considered. This parameter represents a key turbulence scale, describing the balance between buoyant and mechanical production of turbulence. A histogram of L values, grouped by the same $-z_i/L$ classification, provides additional insight into the structure of turbulence under varying convective conditions.

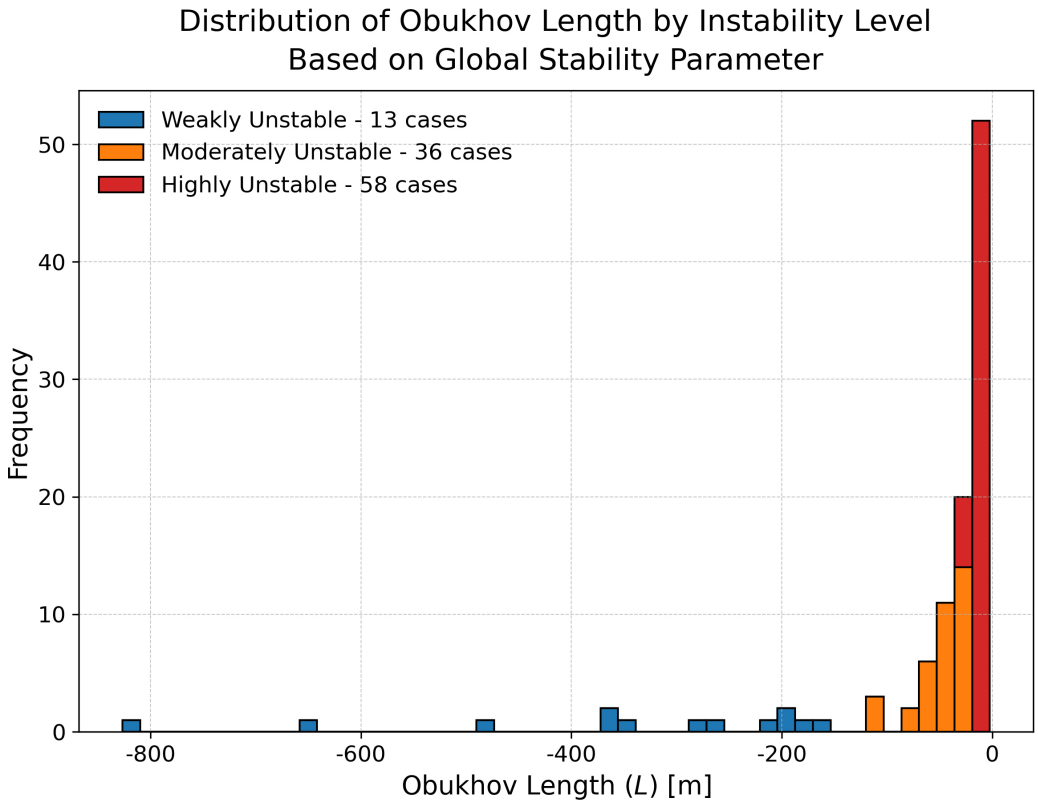

Figure 3.12: Distribution of Obukhov length (L) across observed cases, grouped by stability regime. Weakly unstable (13 cases, blue), moderately unstable (36 cases, orange), and highly unstable (58 cases, red).

To complement the stability-based classification and provide deeper context on surface energy partitioning, Figure 3.13 presents histograms of Bowen ratio (B) and evaporative fraction (E_f). The Bowen ratio is defined as the ratio of sensible to latent

heat flux and can range from 0 to infinity. Lower values of B indicate latent heat dominance (moist surface conditions), while higher values reflect sensible heat dominance (drier surfaces). In contrast, evaporative fraction is constrained between 0 and 1 and represents the proportion of available energy used for evaporation. Values near zero correspond to sensible heat dominance, whereas values near one indicate that most energy is allocated to evaporation.

These distributions provide insight into the variability of surface flux partitioning and its role in modulating boundary layer moisture transport and convective intensity. The E_f histogram exhibits a trimodal distribution, revealing three dominant surface energy partitioning regimes across the dataset. The first peak, located between E_f = 0.1 to 0.3, corresponds to conditions where sensible heat dominates, likely associated with dry surfaces. The second peak, centered around E_f = 0.5 to 0.6, suggests a balanced partitioning between latent and sensible heat fluxes, which may reflect transitional surface moisture conditions. The third peak, near E_f = 0.7 to 1.0, reflects latent heat dominance, indicative of wet surfaces.

This trimodal behavior highlights the heterogeneous nature of surface energy exchange in the SGP region and underscores the influence of land-atmosphere coupling on ABL development. In particular, higher E_f promotes evaporative cooling and enhances near-surface buoyancy fluxes driven by moisture, which can intensify turbulent mixing and deepen the CBL. Conversely, lower E_f restricts latent heat flux, amplifying sensible heat contribution and potentially leading to shallower CBLs. These distinct energy partitioning modes therefore have important implications for moisture transport, convective mixing, and entrainment efficiency.

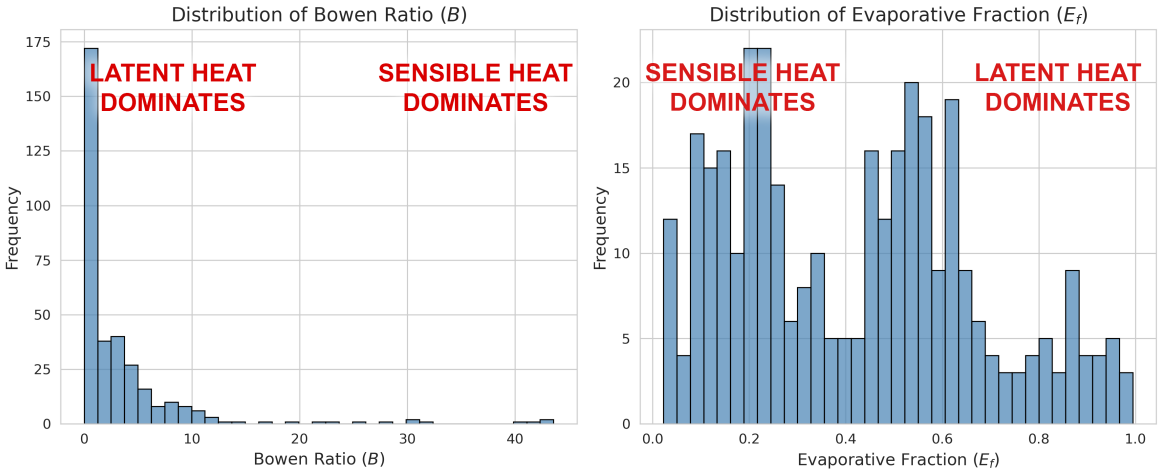

Figure 3.13: Histograms of Bowen ratio (left) and evaporative fraction (E_f, right) for 107 observed cases.

To provide additional context on the structure and behavior of the observational data used in this study, Figure 3.14 presents time-height profiles of vertical velocity, temperature, and water vapor mixing ratio for a representative convective day (August 1, 2018) at the SGP ARM site. Although the core analysis in this study is based on composite statistics across 107 cases, this example offers a visual illustration of the Doppler and Raman lidar data and the characteristic evolution of the CBL over the course of a single day.

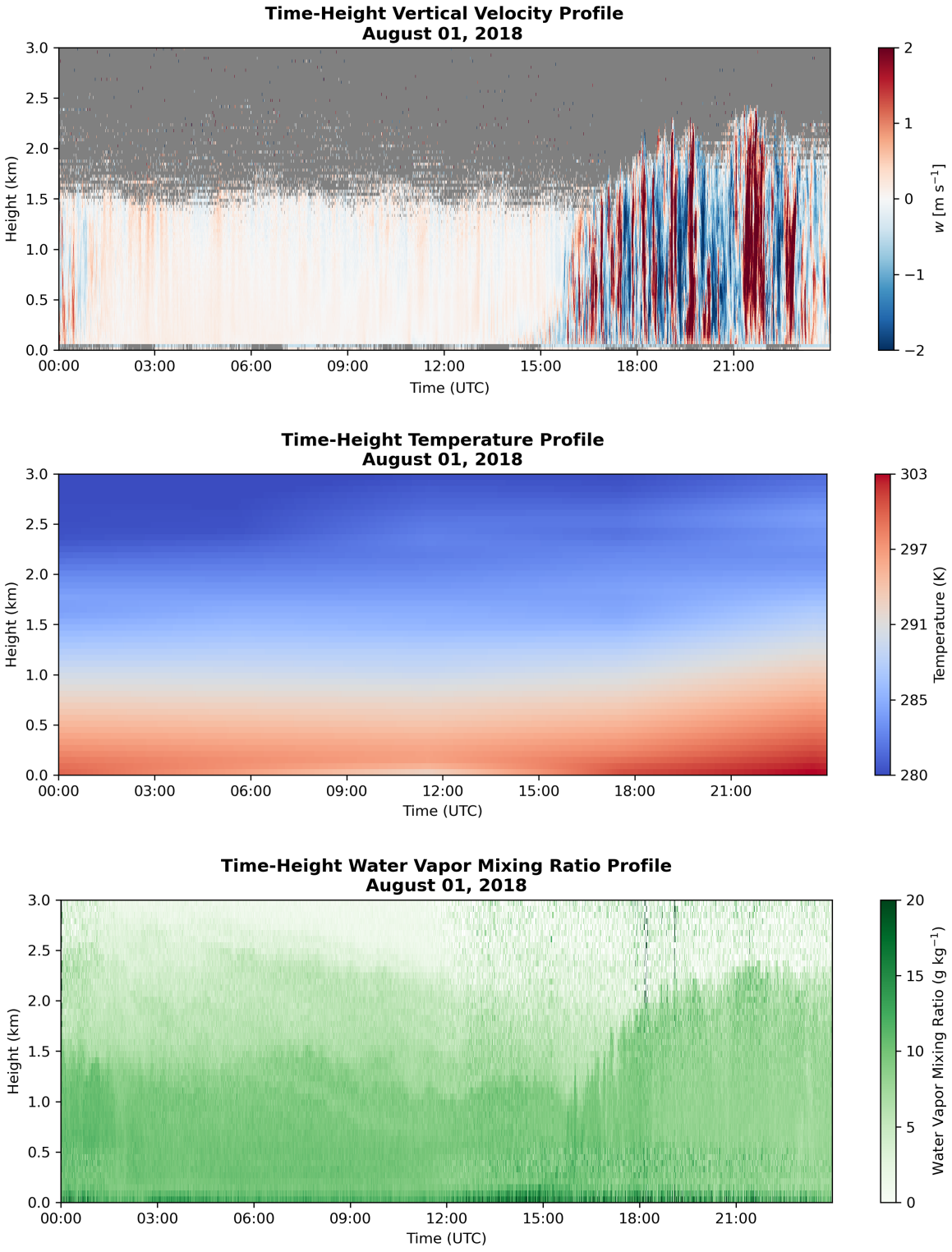

Figure 3.14: Time-Height profiles of vertical velocity (top), temperature (middle), and water vapor mixing ratio (bottom) for August 1, 2018, at the SGP Central Facility.

The vertical velocity plot (Fig. 3.14, top panel) shows intermittent convective activity beginning in the early afternoon and intensifying throughout the late afternoon. The presence of strong updrafts and downdrafts indicate the development of buoyancy-driven turbulent motions, consistent with a deepening CBL under unstable surface conditions.

As part of the data quality control process, Doppler lidar radial velocity was plotted against backscatter intensity to evaluate the reliability of vertical velocity measurements (Fig. 3.15). This comparison allowed for identification of the signal-to-noise characteristics and the detection floor of the instrument. A threshold intensity value of 1.0075 was determined, serving as a reference for distinguishing between valid atmospheric returns and noise. This threshold was applied consistently to filter out unreliable data, ensuring that only high-confidence measurements of vertical velocity were included in the composite and spectral analyses.

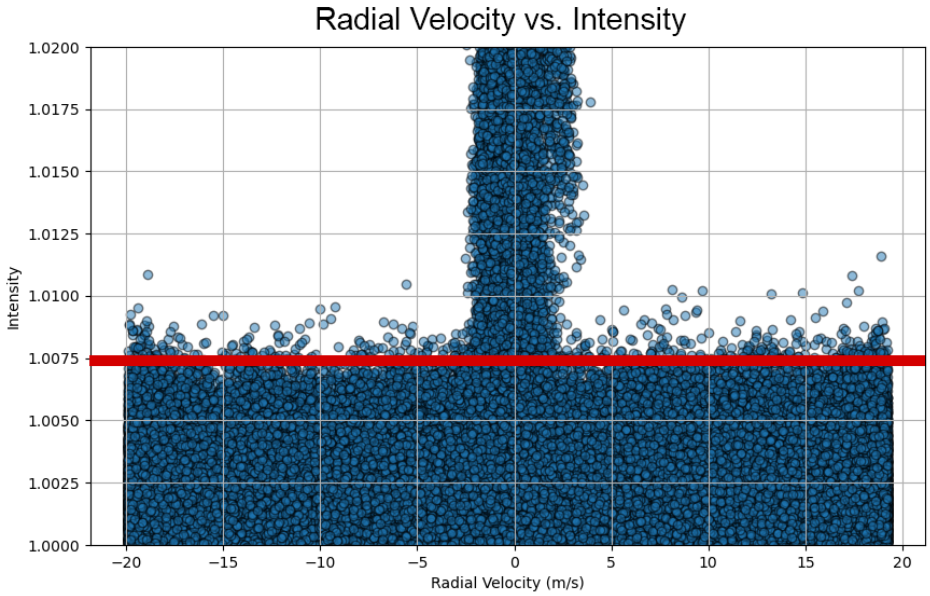

Figure 3.15: Radial velocity plotted against intensity, illustrating the relationship between the two variables. The red line indicates the defined floor level, serving as a reference point for the data.

The middle panel (Fig. 3.14) displays the evolution of temperature with height, highlighting surface heating throughout the day and the associated increase in boundary layer depth. A warming surface and a cooling aloft profile contribute to destabilization and convective development, consistent with the periods of vertical velocity shown above.

The bottom panel (Fig. 3.14) shows the water vapor mixing ratio profile, which remains high in magnitude near the surface through most of the day but gradually becomes more vertically mixed as convective plumes deepen. The afternoon increase in vertical moisture variability coincides with stronger convective activity, suggesting enhanced turbulent mixing and increased entrainment of drier air from above, as well as upward moisture transport from the surface into the upper CBL.

Together, these plots demonstrate the diurnal evolution of the CBL, highlighting the vertical coupling of heat, moisture, and momentum transport during convective conditions. While individual days are not the focus of this research this example illustrates the typical variability observed with the final dataset and sets the stage for the composite-based analysis that follows.

In order to reduce the influence of extreme values on visualizations, particularly for variance profiles and spectrograms, an upper outlier removal method was applied using the interquartile range (IQR) method. For each profile or spectral variable (q, θ, w, and $\overline{w'\theta'}$), values were excluded if they exceeded the upper threshold defined as:

$$\text{Outlier Threshold} = Q_3 + 1.5 \times \text{IQR} \tag{3.10}$$

where Q_3 is the third quartile and IQR $= Q_3 - Q_1$ is the interquartile range. This filtering was applied only to the figures (e.g., spaghetti plots and composite spectrograms, shown in Section 4) to reduce distortion from extreme values and better highlight dominant structural features.

In addition, summary tables of the highly, moderately, and weakly unstable cases are provided in the Appendix (Tables A.1, A.2, and A.3). Each table lists the date, hour, ABL depth (z_i), Obukhov length (L), global stability parameter ($-z_i/L$), and convective velocity scale (w_*) for the cases used in the analysis. These tables offer context for interpreting the composite profiles and support reproducibility of the results.

Chapter 4

Results

4.1 Time-Height Structure of Heat and Moisture Transport

To characterize the range of surface energy partitioning and atmospheric stability conditions encompassed by our dataset, we examine the joint probability density function (PDF) of E_f and $-z_i/L$. Together, these two parameters define the primary thermodynamic parameter space governing scalar transport in the CBL (see Section 2.3).

Figure 4.1 shows the joint PDF across all analyzed cases. The distribution reveals a broad spread in E_f, ranging from 0 to 1, with three primary modes centered around low (~ 0.2), moderate (~ 0.5), and high (~ 0.8) evaporative fraction numerical values, indicating a trimodal distribution. These clusters appear alongside varying degrees of atmospheric instability, as quantified by $-z_i/L$.

Higher values of E_f, which reflect a greater proportion of latent heat flux relative to total surface energy, are generally associated with weaker instability (small z_i/L). Conversely, lower E_f values, indicative of sensible heat dominance, tend to correspond to more unstable conditions (large z_i/L). Histograms along the top and side of the plot show the individual distributions of E_f and $-z_i/L$, respectively. The computed linear correlation coefficient between E_f and $-z_i/L$ is -0.23, indicating a weak negative association across the dataset. However, despite this slight negative correlation, the

dataset includes essentially all possible combinations of E_f and $-z_i/L$, such that cases with low $-z_i/L$ and low E_f, as well as high E_f and high $-z_i/L$, are present, ensuring a comprehensive coverage of the joint parameter space.

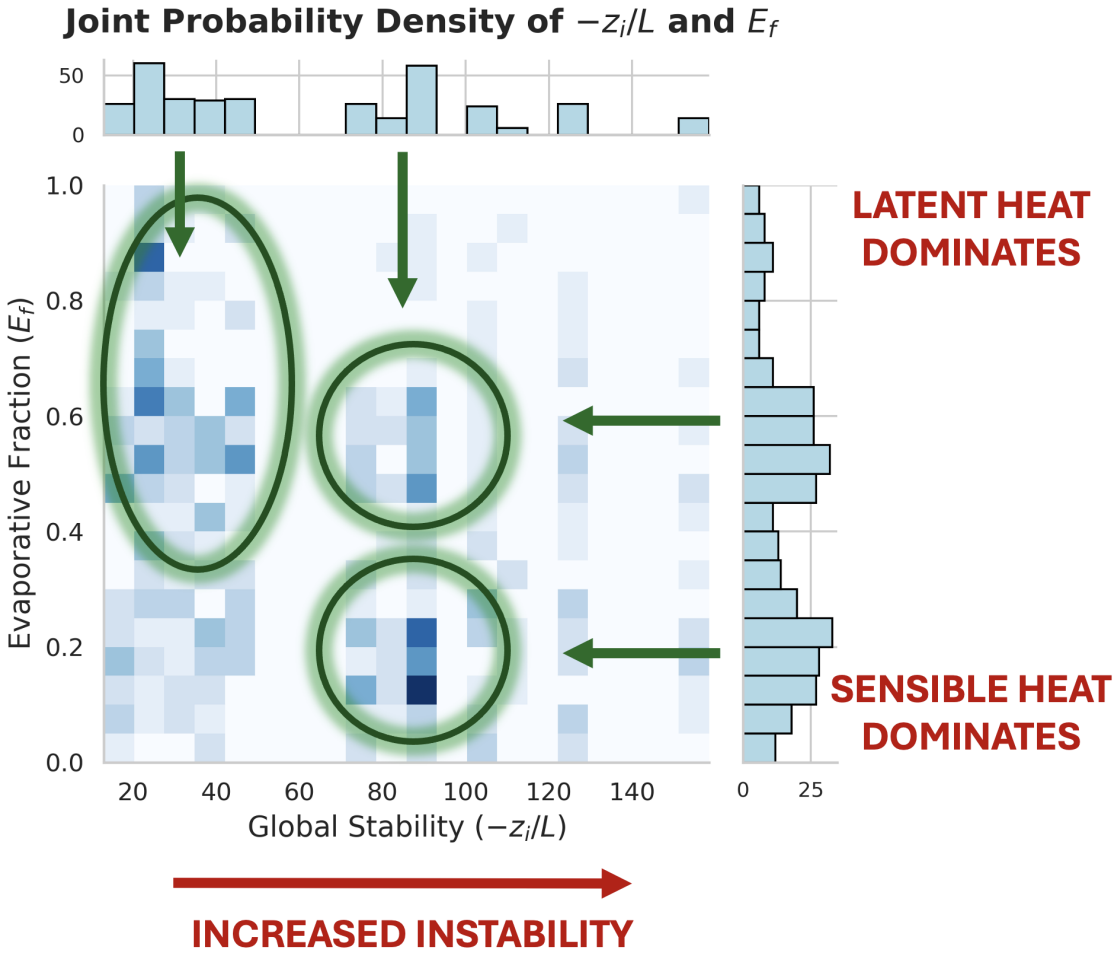

Figure 4.1: Joint probability density function (PDF) of evaporative fraction (E_f) and global stability parameter ($-z_i/L$) for the final 107 cases. Marginal histograms show the individual distributions of each variable.

4.2 Vertical Structure of Scalar Variability

To assess how turbulent transport of heat and moisture varies with instability, Figures 4.2, 4.4, 4.6, and 4.8 present vertical profiles of normalized scalar flux variance

and covariance across three stability regimes: highly unstable, moderately unstable, and least unstable. Each panel includes line plots of individual hourly cases, along with composite means with shaded regions denoting one and two standard deviations from the mean.

Figures 4.3, 4.5, 4.7, and 4.9 show the corresponding composite mean profiles of normalized scalar flux variance and covariance, with the three stability regimes overlaid for direct comparison. This side-by-side visualization highlights structural differences in vertical flux variability as a function of convective strength.

Note that upper outliers were removed using the IQR method prior to generating these profiles to better emphasize the dominant structure and reduce skew from extreme cases, as discussed in Section 3.4.

4.2.1 Vertical Velocity Variance

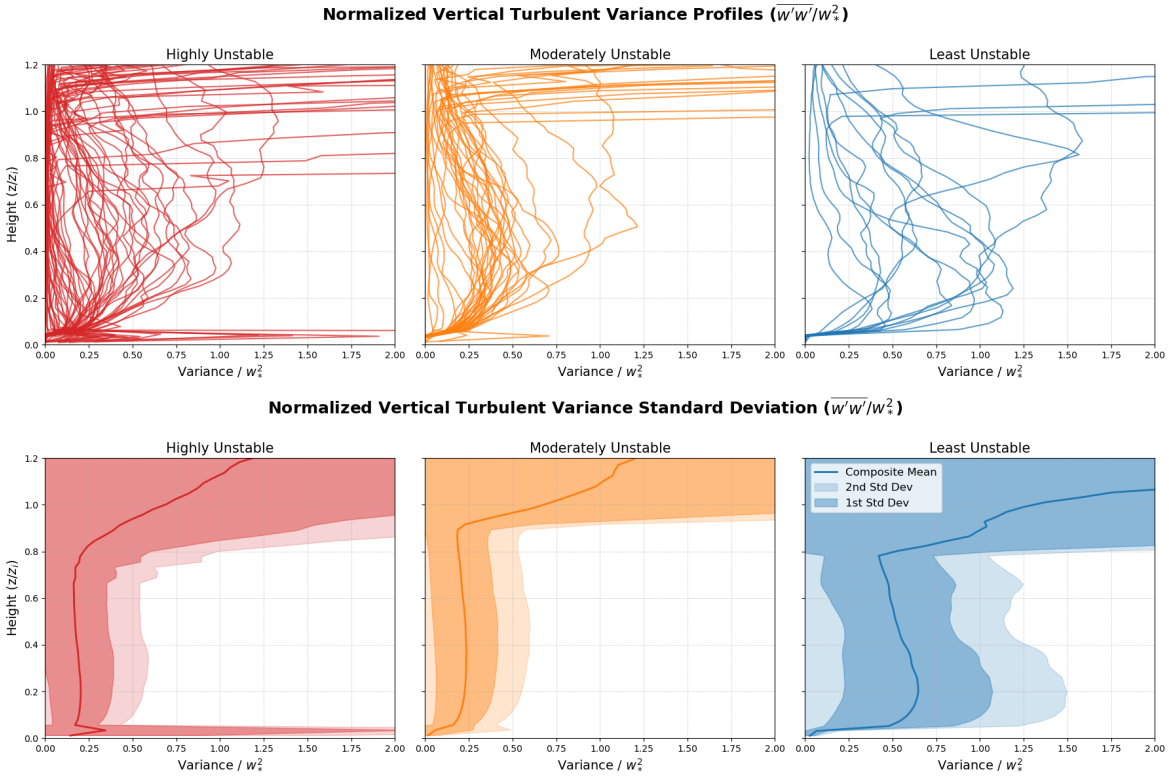

Figure 4.2: Normalized vertical velocity variance profiles $\overline{w'w'}/w_*^2$ as a function of normalized height z/z_i across three instability regimes. Individual lines represent hourly cases (top); shaded regions denote one and two standard deviations from the composite mean (bottom).

Figure 4.2 displays normalized vertical velocity variance $\overline{w'w'}/w_*^2$, highlighting the dynamical structure of turbulence. Once the IQR test was complete, there were no outliers for the vertical velocity variance. In all regimes, variance peaks near the surface and again in the upper mixed layer, consistent with the presence of large-scale convective plumes and entrainment zones. However, the amplitude of variance is significantly greater in highly unstable conditions, and the profiles exhibit more vertical coherence.

Highly unstable profiles show vertically extended peaks and tight clustering in the mid-CBL, indicative of deep, organized vertical motion. Moderately unstable profiles

display broader spread, while the least unstable cases show a diffuse and flattened structure, consistent with less coherent vertical transport. These patterns reaffirm that the vigor and spatial coherence of vertical motions are closely tied to surface heating and convective strength.

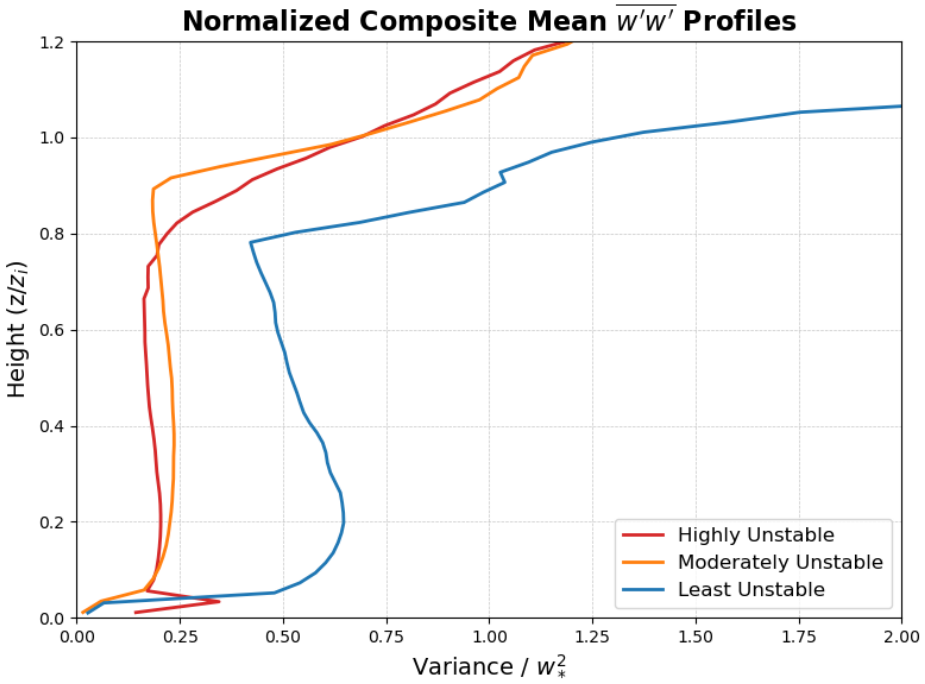

Figure 4.3: Normalized composite mean vertical velocity variance profiles for highly, moderately, and least unstable cases.

In Figure 4.3, vertical profiles of normalized vertical velocity variance exhibit clear differences in structure and amplitude across stability regimes. Under highly unstable conditions, the normalized variance reaches its maximum values, with a broad peak centered between $z/z_i \approx 0.3$ and 0.5. This pattern reflects deep convective plumes generated by strong surface heating. Despite these elevated values, the spread between individual cases is relatively narrow, indicating that vertical velocity fluctuations are more consistent in magnitude under strong convective forcing. This suggests that buoyancy-driven turbulence organizes vertical motions more uniformly in the highly unstable regime.

In contrast, the moderately and least unstable regimes show both a reduction in the peak amplitude and a downward shift in the altitude of maximum variance. For these cases, variance peaks closer to the surface and decays more rapidly with height, consistent with shallower, less vigorous convective updrafts. The increased variability among individual profiles under weaker forcing also highlights the influence of transient or local heterogeneities that may disrupt coherent plume formation. Overall, the vertical velocity variance structure confirms the dominant role of surface buoyancy in shaping the depth and intensity of convective turbulence within the CBL.

4.2.2 Moisture Variance

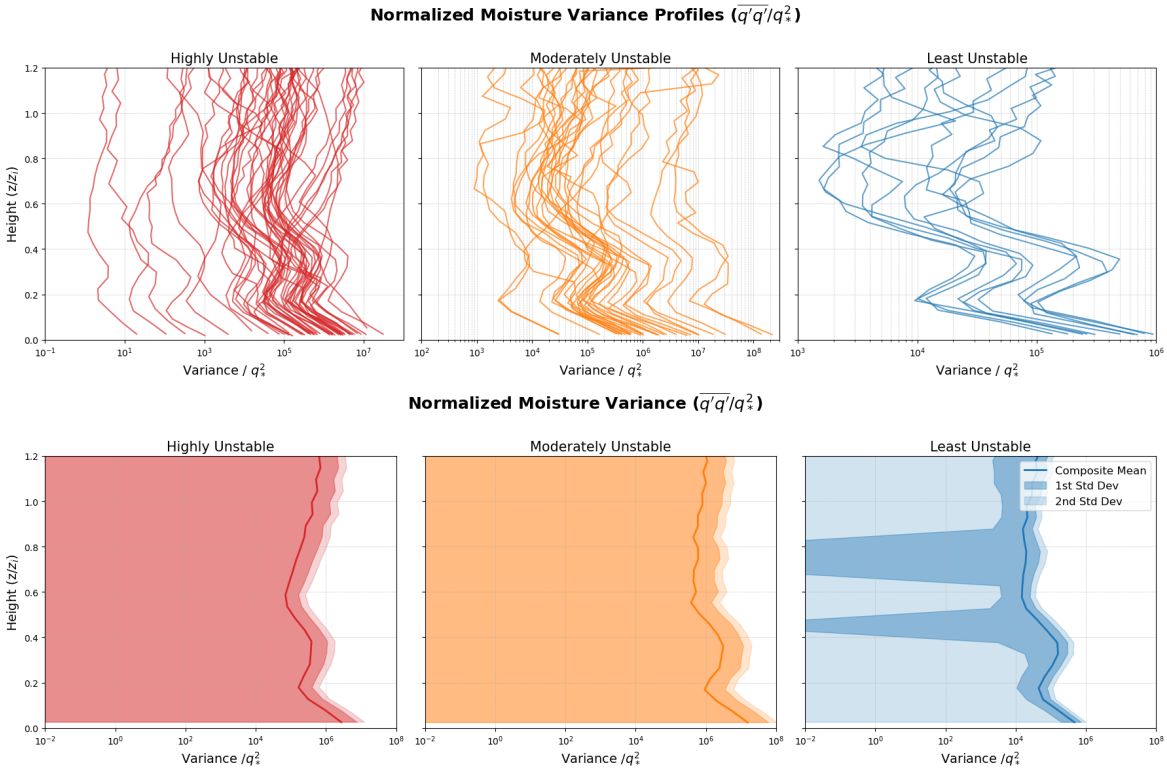

Figure 4.4: As in Fig. 4.2, but for normalized moisture flux profiles $\overline{q'q'}/q_*^2$ as a function of normalized height z/z_i across three instability regimes.

Profiles of normalized moisture variance (Figure 4.4), show a sensitivity to atmospheric stability, with individual cases exhibiting substantial variability in both structure and magnitude. Once the IQR test was complete, there were 18 identified outliers (highly unstable = 9 cases, moderately unstable = 6, least unstable = 3 cases) for the moisture variance. In the spaghetti plots, a strong near-surface confinement of moisture variance is evident across all regimes, with the bulk of the variance concentrated below $z/z_i \approx 0.4$. This behavior reflects the limited vertical penetration of humidity fluctuations, which are strongly tethered to surface evaporation processes and are less efficiently transported upward than temperature or momentum.

Under highly unstable conditions, values are generally larger near the surface, indicative of enhanced vertical mixing and greater moisture availability. However, despite stronger convective activity, these cases do not exhibit a correspondingly broad vertical distribution of variance. Instead, moisture fluctuations remain confined to the lower half of the CBL, suggesting that entrainment and moisture dilution near the inversion play a limiting role. Standard deviation shading reveals a relatively narrow spread near the surface, particularly under highly unstable conditions, pointing to more consistent moisture variance structure in these regimes. In contrast, both moderate and least unstable conditions exhibit broader spreads in the variance profiles, reflecting increased case-to-case variability and greater sensitivity to surface heterogeneity and local flux conditions.

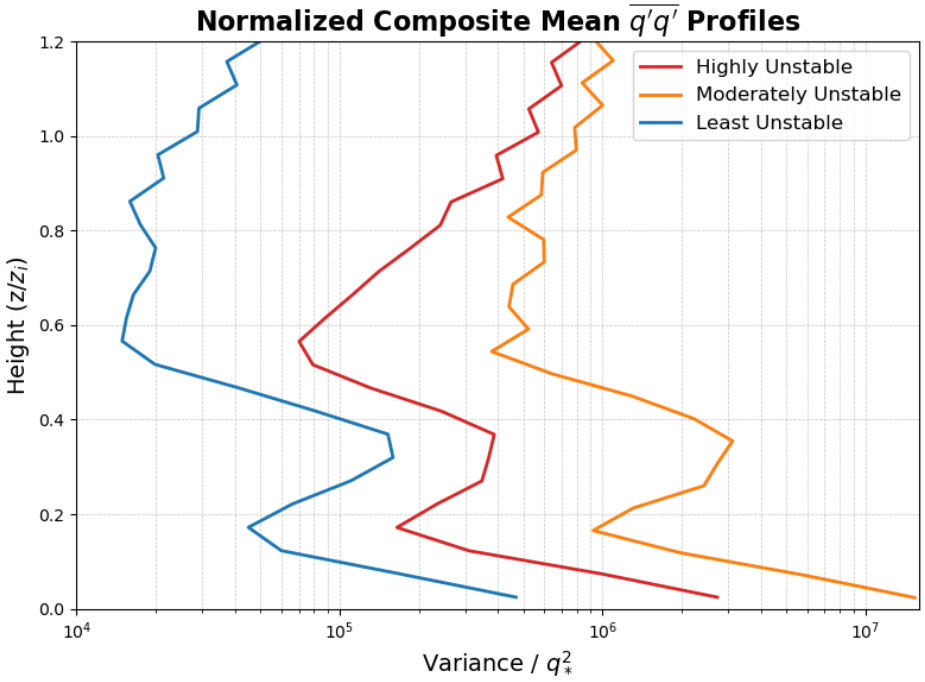

Figure 4.5: As in Fig. 4.3, but for moisture variance.

Composite mean profiles of normalized moisture variance across the three stability regimes reinforce these structural patterns and highlight systematic shifts in vertical

organization with increasing instability. In the least unstable regime remains confined to a shallow layer near the surface, with variance rapidly declining above $z/z_i \approx 0.2$. This suggests that weak surface forcing is insufficient to generate deep turbulent mixing of moisture, leading to stratified and moisture-limited conditions in the upper CBL.

As instability increases, the composite profiles shift upward and modestly broaden, indicating slightly deeper mixing and greater moisture variability aloft. Under highly unstable conditions, the composite mean profile exhibits its highest near-surface values and a more gradual decay with height, extending up to $z/z_i \approx 0.5$. However, even in this regime, the vertical extent of humidity variance remains more limited compared to temperature or velocity variance, emphasizing the more passive, surface-bound behavior of moisture as a scalar.

Collectively, these results demonstrate that while instability enhances near-surface moisture variability, the vertical confinement of $\overline{q'q'}$ remains a persistent feature of the CBL. This reflects both the conservative nature of water vapor in the absence of strong entrainment and the differential transport efficiency between active (temperature) and passive (humidity) scalars.

4.2.3 Temperature Variance

Figures 4.6 and 4.7 illustrate the vertical structure of normalized temperature variance across the three stability regimes. Once the IQR test was complete, there were 17 identified outliers (highly unstable = 8 cases, moderately unstable = 6, least unstable = 3 cases) for the temperature variance. The spaghetti plots in Figure 4.6 reveal clear regime-dependent differences in both magnitude and vertical extent. Under highly unstable conditions, the profiles are consistently elevated, with peak values occurring between $z/z_i \approx 0.3$ and 0.5. These profiles also display a broader vertical distribution,

extending to higher altitudes within the boundary layer, indicative of strong vertical mixing and enhanced thermal fluctuations driven by robust convective updrafts.

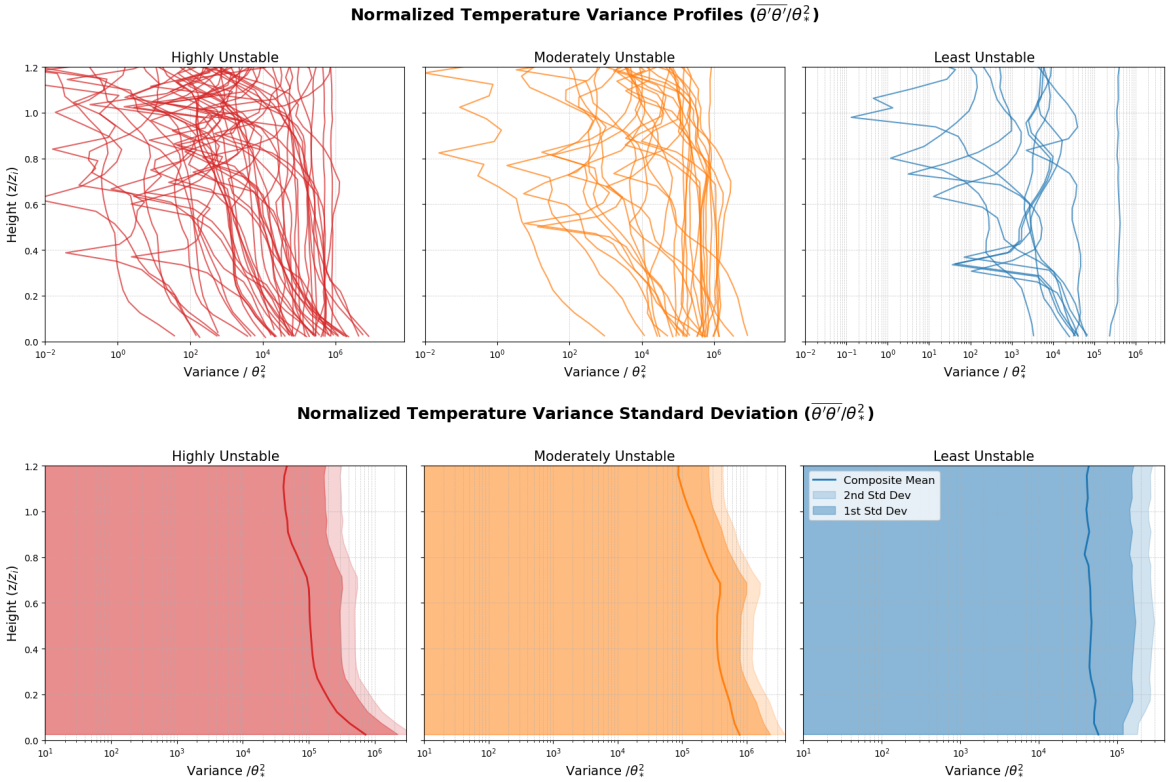

Figure 4.6: As in Fig. 4.2, but for normalized temperature flux profiles $\overline{\theta'\theta'}/\theta_*^2$ as a function of normalized height z/z_i across three instability regimes.

In contrast, temperature variance profiles under moderately and weakly unstable conditions exhibit lower magnitudes and a more confined vertical extent. The least unstable regime shows the narrowest spread in the ensemble of profiles and the lowest composite mean values, reflecting weaker convective intensity and reduced thermal turbulence. The shaded regions representing one and two standard deviations are widest under highly unstable conditions, suggesting greater case-to-case variability and stronger dependence on mesoscale forcing or boundary conditions.

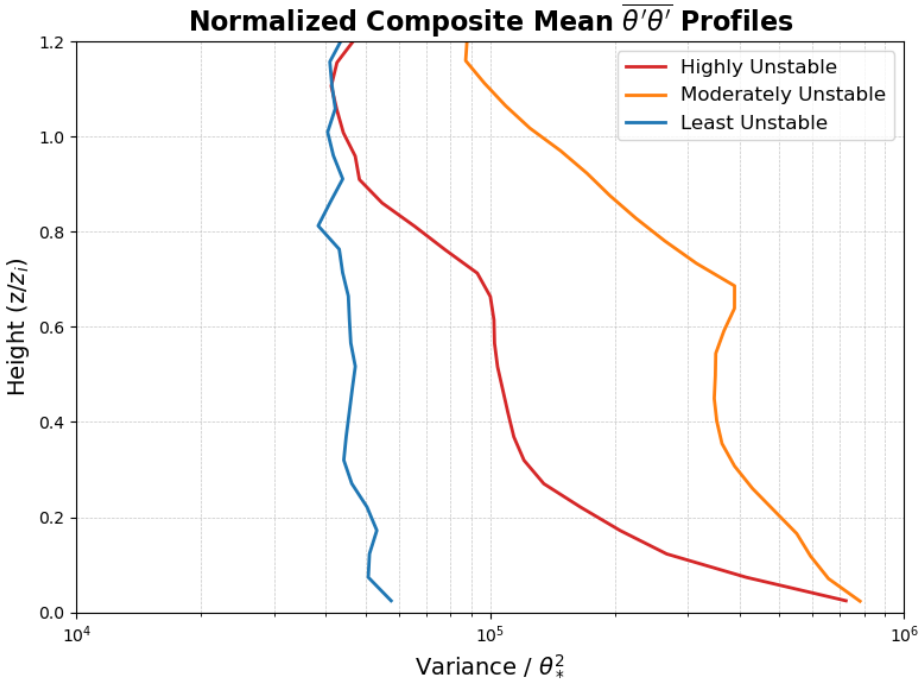

Figure 4.7: As in Fig. 4.3, but for temperature variance.

Normalized temperature variance exhibits a distinct vertical structure that varies with convective regime. The moderately unstable composite displays the highest peak in variance, centered near $z/z_i \approx 0.7$, suggesting strong thermal fluctuations and potential enhancement by entrainment processes near the inversion. The highly unstable regime shows a slightly lower peak around $z/z_i \approx 0.6$, but with a broader vertical distribution that reflects more deeply mixed thermal structures. In contrast, the least unstable regime is marked by weak variance confined to the lower boundary layer, indicating limited vertical mixing. These results challenge the assumption that stronger surface instability always produces the highest normalized temperature variance, instead pointing to a complex interplay between surface fluxes, entrainment, and boundary layer depth. This underscores the importance of incorporating regime-dependent structure into turbulence parameterizations for accurate scalar transport modeling.

4.2.4 Temperature-Humidity Covariance

Figures 4.8 and 4.9 display the vertical profiles of normalized temperature–humidity covariance across three convective regimes. Once the IQR test was complete, there were 17 identified outliers (highly unstable = 8 cases, moderately unstable = 6, least unstable = 3 cases) for the temperature–humidity covariance. These profiles characterize the co-variability between temperature and humidity fluctuations and provide insight into scalar coupling and mixing mechanisms in the CBL.

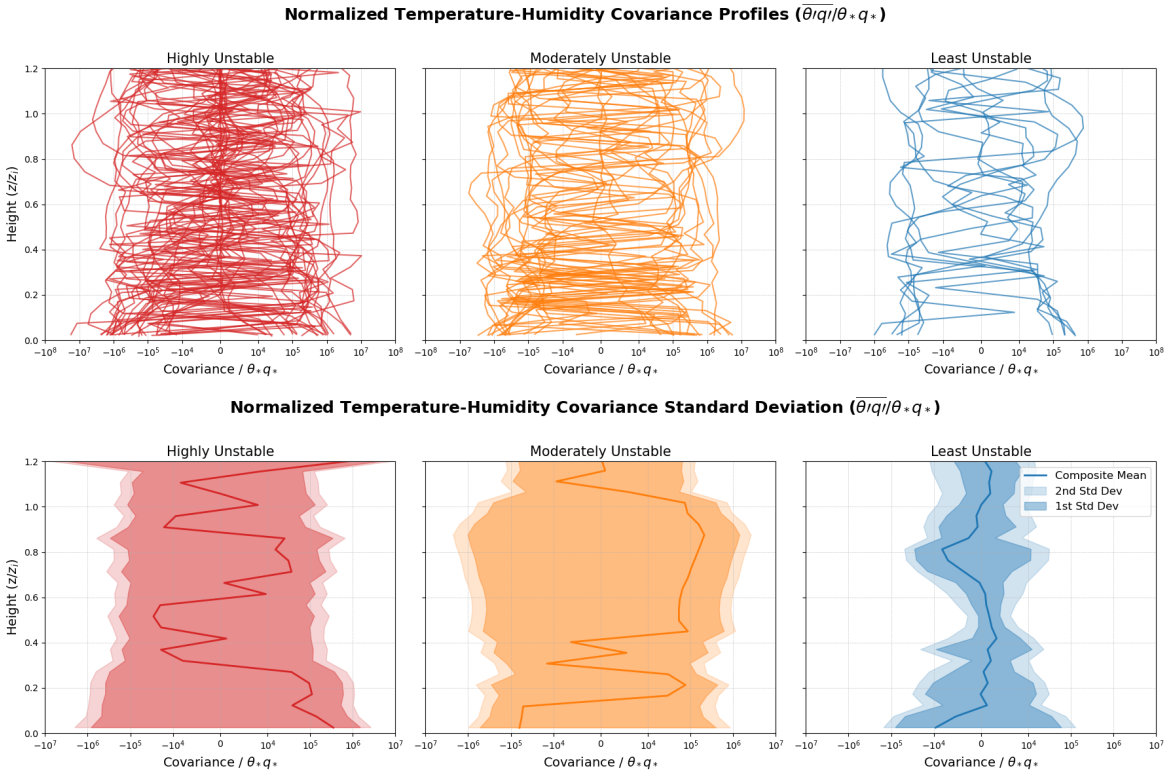

Figure 4.8: As in Fig. 4.2, but for normalized temperature–humidity flux profiles, $\overline{\theta' q'}/\theta_* q_*$, as a function of normalized height z/z_i across three instability regimes.

In the highly unstable regime, the covariance exhibits the most pronounced and vertically extensive structure. Individual profiles display consistently positive covariance, with the strongest values occurring between $z/z_i \approx 0.2$ and 0.6. The composite mean remains relatively constant with height throughout the well-mixed layer, confirming strong and persistent scalar coupling. Importantly, the spread among individual profiles is relatively narrow compared to the other regimes, as indicated by the tight standard deviation bands, reflecting a robust and consistent relationship between temperature and humidity under vigorous convective forcing.

The moderately unstable regime shows intermediate behavior. Profiles are more variable and less vertically extensive than in the highly unstable case, and the composite mean displays a modest peak near $z/z_i \approx 0.4$ before tapering with height. While positive covariance is still present in most profiles, the increased variability and broader standard deviation bands suggest greater case-to-case differences in scalar coupling. This may reflect sensitivity to boundary-layer depth, surface flux heterogeneity, or residual stratification in less convective conditions.

Under least unstable conditions, the structure breaks down substantially. Individual profiles are highly variable, and many approach zero or switch sign, indicating the absence of consistent co-transport. The composite mean remains weakly positive and shallow, peaking around $z/z_i \approx 0.2$, but rapidly decays with height. The broad standard deviation envelopes underscore significant variability in both magnitude and sign, highlighting the reduced coherence in temperature–humidity interactions in weakly convective environments.

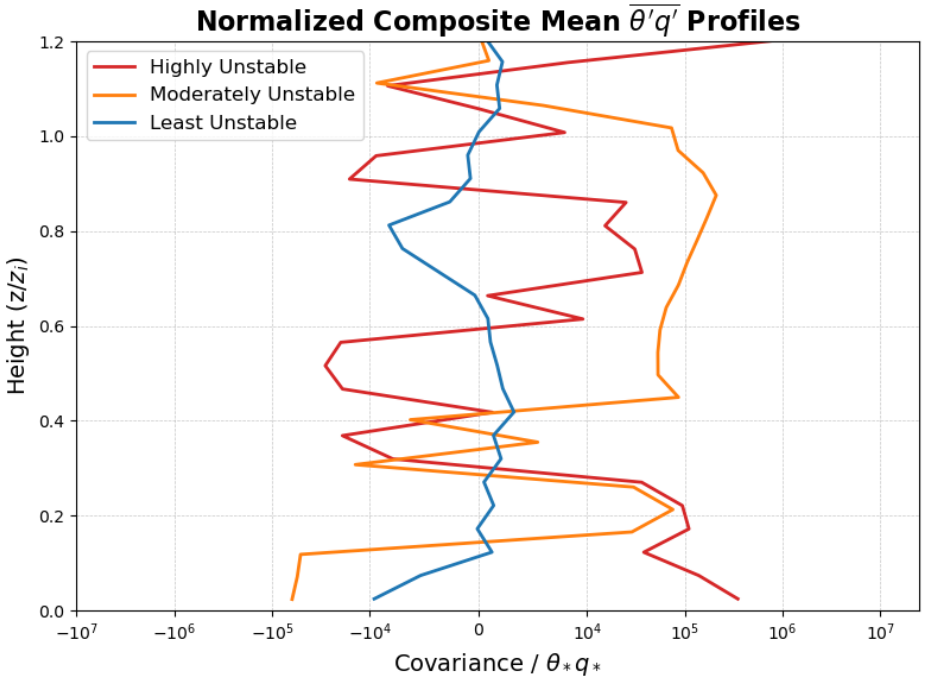

Figure 4.9: As in Fig. 4.3, but for temperature–humidity variance.

The composite mean profiles in Figure 4.9 illustrate the vertical structure of normalized temperature–humidity covariance across different stability regimes. Under highly unstable conditions, the covariance is predominantly positive and extends through a large portion of the boundary layer, with peak values centered between $z/z_i \approx 0.2$ and 0.7. This pattern suggests strong and coherent transport of temperature and moisture by convective updrafts and downdrafts. The moderately unstable profile also exhibits positive covariance, but with slightly reduced magnitude and more mid-level concentration, indicative of somewhat weaker but still organized coupling between buoyancy and humidity fields.

In contrast, the least unstable regime exhibits a disorganized covariance structure, with values that fluctuate around zero and alternate in sign throughout the boundary layer. This pattern indicates a weak and inconsistent coupling between temperature and humidity fluctuations, likely resulting from diminished convective vigor and less

coherent turbulent structures. Rather than exhibiting coordinated vertical transport, scalar interactions in this regime appear fragmented and inefficient. These findings emphasize that stronger convective instability enhances the coherence and magnitude of scalar covariance, highlighting the importance of representing variable thermodynamic coupling in turbulence parameterizations across different stability regimes.

4.3 Spectral Characteristics of Vertical Velocity Fluctuations

To interpret the vertical and spectral distribution of turbulence within the CBL, it is useful to examine variability as a function of normalized wavelength (λ/z_i) and normalized height (z/z_i). This two-dimensional framework captures how turbulent energy is organized across spatial scales and vertical levels within the boundary layer. Figure 4.10 presents a conceptual schematic of this spectral domain. The vertical axis (y-axis) denotes λ/z_i, which separates small-scale motions (SSMs, $\lambda/z_i < 1$) from LSMs ($\lambda/z_i > 1$), while the horizontal axis (x-axis) represents increasing height normalized by the boundary layer depth. The dashed line at $\lambda/z_i = 1$ provides a reference threshold distinguishing motions larger and smaller than the depth of the CBL. This framework forms the basis for interpreting the composite spectrograms that follow.

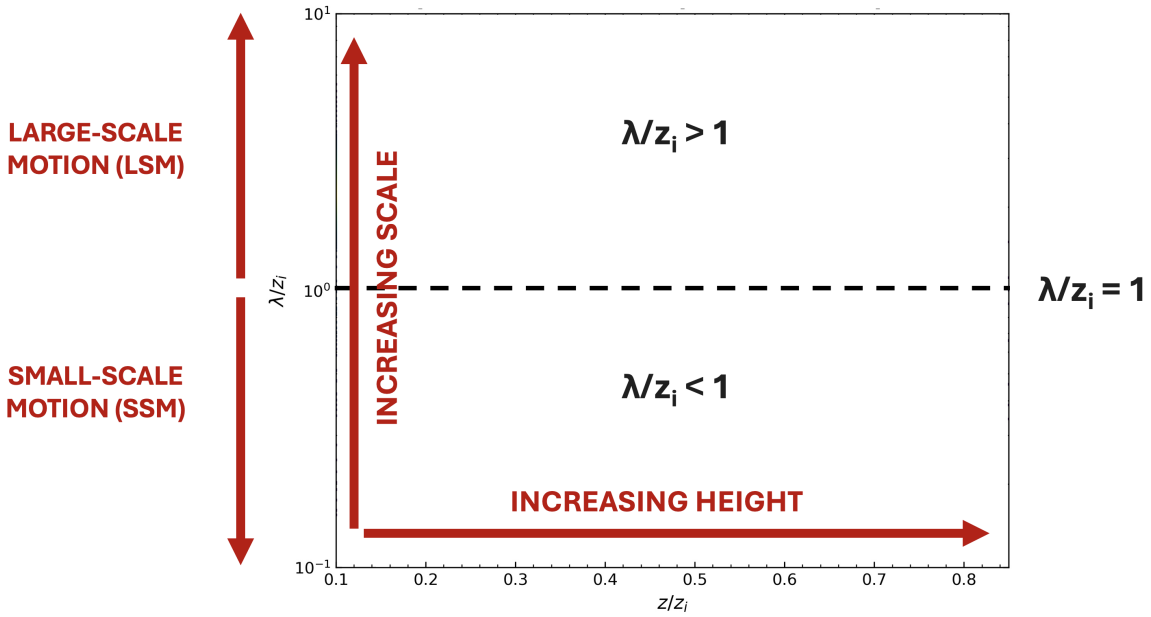

Figure 4.10: Schematic illustrating the spectral domain used for analysis of turbulent motions in the CBL. The y-axis shows the normalized wavelength (λ/z_i), with $\lambda/z_i > 1$ representing LSMs and $\lambda/z_i < 1$ representing small-scale motions (SSMs). The x-axis denotes normalized height (z/z_i). The dashed line at $\lambda/z_i = 1$ separates contributions from LSMs and SSMs while indicating the scale of the CBL. Arrows indicate increasing scale (vertical) and increasing height (horizontal) within the CBL.

To provide a baseline characterization of vertical velocity structure across the entire dataset, Figure 4.11 shows the composite mean vertical velocity spectrum for all 107 analyzed cases. This plot aggregates data across all stability regimes, offering a generalized view of the vertical and spectral distribution of turbulent energy in the vertical velocity component.

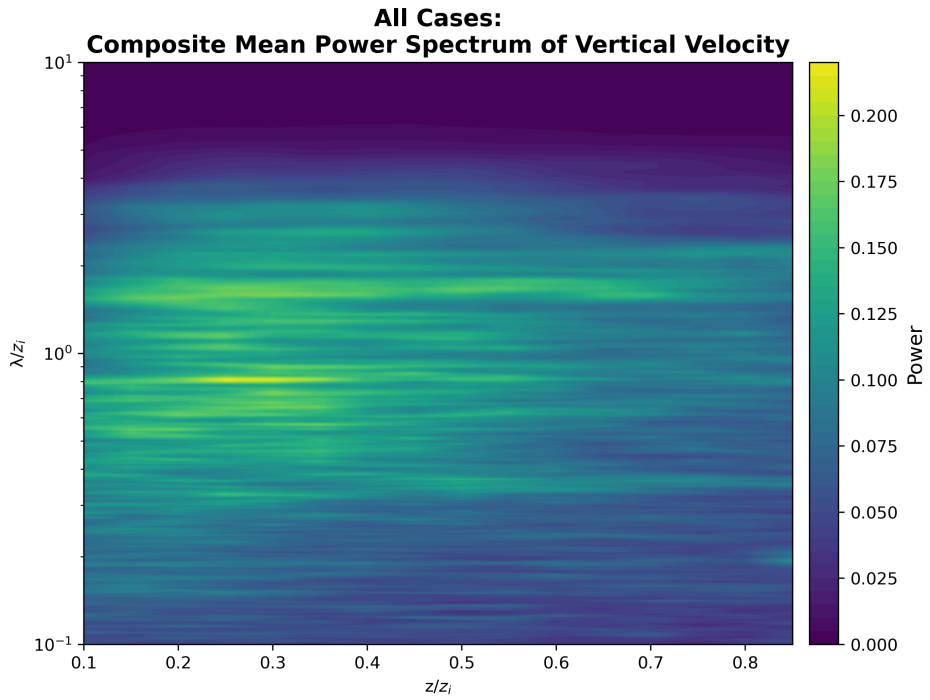

Figure 4.11: Composite mean spectrograms of vertical velocity for all cases, excluding outliers. Non-dimensional height (z/z_i) is on the x-axis, and non-dimensional wavelength (λ/z_i) is on the y-axis. Color shading indicates spectral power.

The spectrum reveals a dominant peak near $\lambda/z_i \approx 1$ and $z/z_i \approx 0.3$, suggesting that vertical motions with scales comparable to the boundary layer depth are prevalent throughout the dataset. Spectral energy is broadly distributed across both scale and height, though generally lower in magnitude than in the highly unstable subset. This distributions indicates that large-scale vertical velocity structures are a common feature in the CBL, even when averaged over a wide range of convective conditions.

Figure 4.12 shows composite mean power spectrograms of vertical velocity for three different convective stability regimes: highly unstable, moderately unstable, and weakly unstable. Each panel illustrates how spectral power varies as a function of normalized height and normalized wavelength.

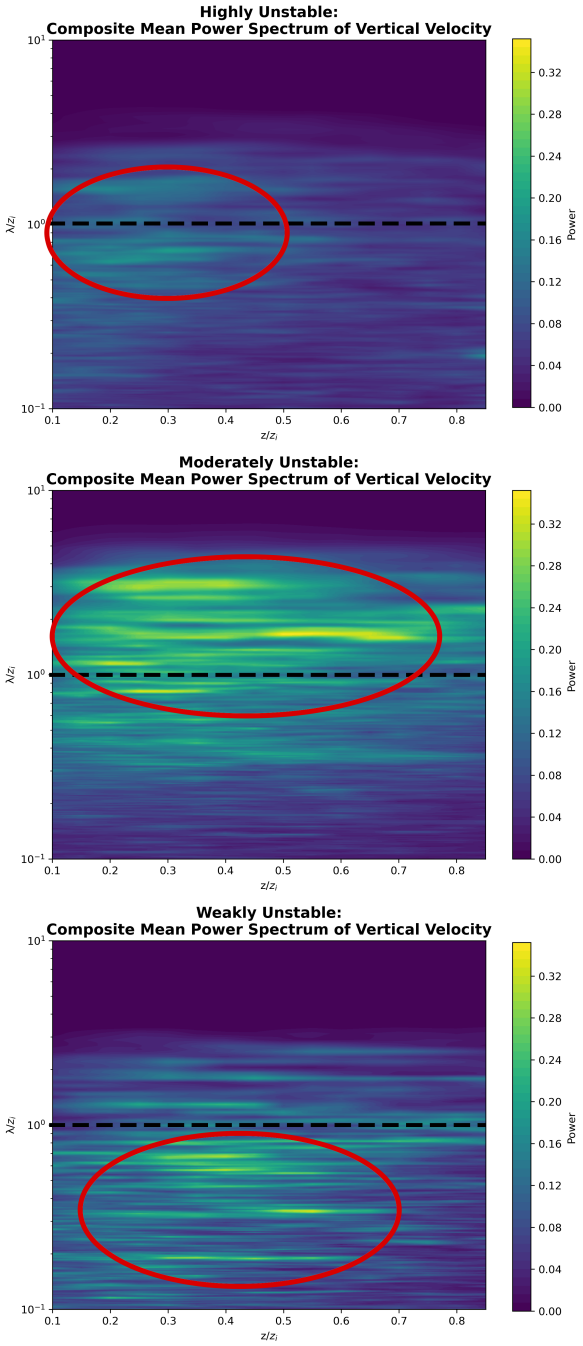

Figure 4.12: Composite mean spectrograms of vertical velocity variance for highly (top), moderately (middle), and weakly unstable (bottom) regimes. The x-axis shows non-dimensional height (z/z_i) and the y-axis shows non-dimensional wavelength (λ/z_i). Color shading indicates spectral power.

In the highly unstable regime, spectral energy is distributed throughout the mixed layer, with weak power evident across a wide range of scales. Energy is present both at smaller wavelengths ($\lambda/z_i < 1$), particularly near the surface, and at wavelengths on the order of the boundary layer depth ($\lambda/z_i \approx 1$). This distribution reflects the presence of both localized turbulence and coherent LSMs contributing to vertical mixing.

The moderately unstable regime exhibits a more concentrated pattern of spectral energy, with a LSM outer peak circled in red. Power remains elevated but is more focused around $\lambda/z_i \approx 1$ and $z/z_i \approx 0.5 - 0.7$, indicating the presence of dominant boundary-layer-scale structures in the upper half of the CBL.

In the weakly unstable regime, spectral energy is noticeably weaker and more confined to lower altitudes and smaller wavelengths (SSMs). The highest power is concentrated below $z/z_i = 0.5$, with minimal energy at larger scales. This pattern is consistent with weaker convective forcing and reduced vertical development of turbulence, reflecting suppressed buoyancy production and enhanced shear influence.

4.4 Spectral Characteristics of Heat and Moisture Fluctuations

4.4.1 Composite Mean Spectrograms of Temperature and Humidity

To establish a baseline understanding of scalar variability within the CBL, composite mean spectrograms of temperature and humidity were generated using all 107 analyzed cases, regardless of stability classification. These spectrograms display the distribution of variance as a function of normalized height (z/z_i) and normalized wavelength (λ/z_i), allowing for scale- and height-dependent comparisons between the two scalars.

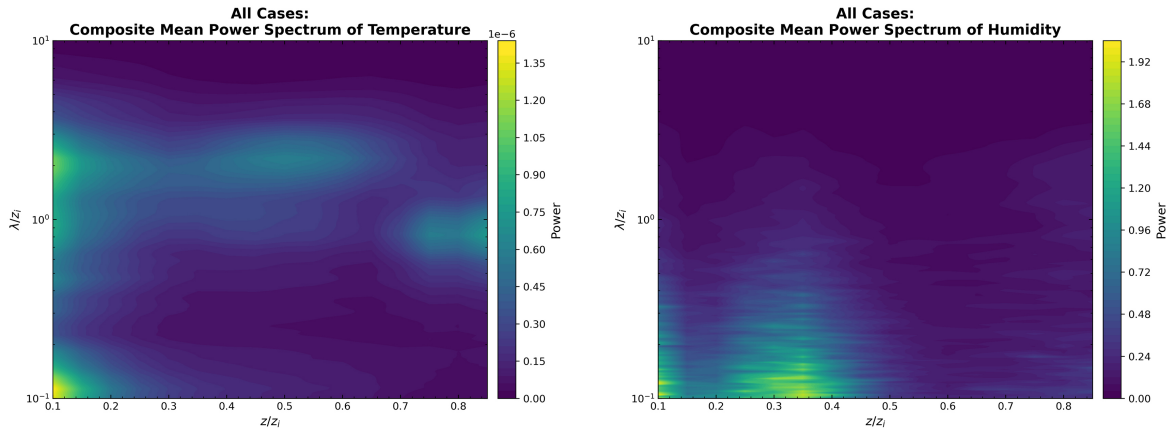

Figure 4.13: Composite mean spectrograms of temperature (left) and humidity (right) for all cases, excluding outliers. Non-dimensional height (z/z_i) is on the x-axis, and non-dimensional wavelength (λ/z_i) is on the y-axis. Color shading indicates spectral power.

The composite temperature spectrum reveals distinct peaks near $\lambda/z_i \approx 1$, particularly between $z/z_i = 0.3$ and 0.7, indicating enhanced power at scales comparable to the depth of the boundary layer. This structure reflects the influence of large-scale motions that contribute substantially to heat transport throughout the CBL. Elevated energy is also present at smaller scales near the surface, consistent with localized turbulence driven by buoyant production.

In contrast, the composite humidity spectrum exhibits a dominant spectral peak around $z/z_i = 0.35$. Power is more vertically confined and concentrated below $z/z_i = 0.4$, with energy primarily at shorter wavelengths ($\lambda/z_i < 1$). This suggests that water vapor fluctuations are more localized, with weaker contributions from boundary-layer-scale structures. Overall, temperature exhibits a deeper and broader vertical reach, while humidity variability is more limited in both scale and altitude.

4.4.2 Temperature Spectral Analysis by Stability Regime

To explore how scalar structure evolves with atmospheric instability, composite mean temperature spectrograms were generated for highly, moderately, and weakly unstable regimes based on the global stability parameter $-z_i/L$ (Figure 4.14).

In highly unstable conditions, temperature variance is broadly distributed across both large and small scales throughout the CBL. Small-scale energy ($\lambda/z_i < 1$) is strongest near the surface ($z/z_i < 0.2$), reflecting intense local turbulence. At the same time, elevated energy at $\lambda/z_i \approx 1$ appears in both the lower and upper CBL, consistent with the presence of large-scale convective structures that span much of the boundary layer depth.

Under moderately unstable conditions, temperature fluctuations are concentrated near the surface, with spectral energy decreasing significantly with height. This suggests that turbulence is less efficient at redistributing heat vertically and that LSMs are less dominant than in highly unstable cases.

In weak instability regimes, temperature variance shifts toward larger scales ($\lambda/z_i > 1$) and is concentrated in the mid-layer ($z/z_i < 0.3$ and $0.4 < z/z_i < 0.7$), indicating that energy is dominated by horizontally extensive structures with limited vertical development. The lack of small-scale energy and the confinement of fluctuations reflect suppressed mixing and weaker convective forcing.

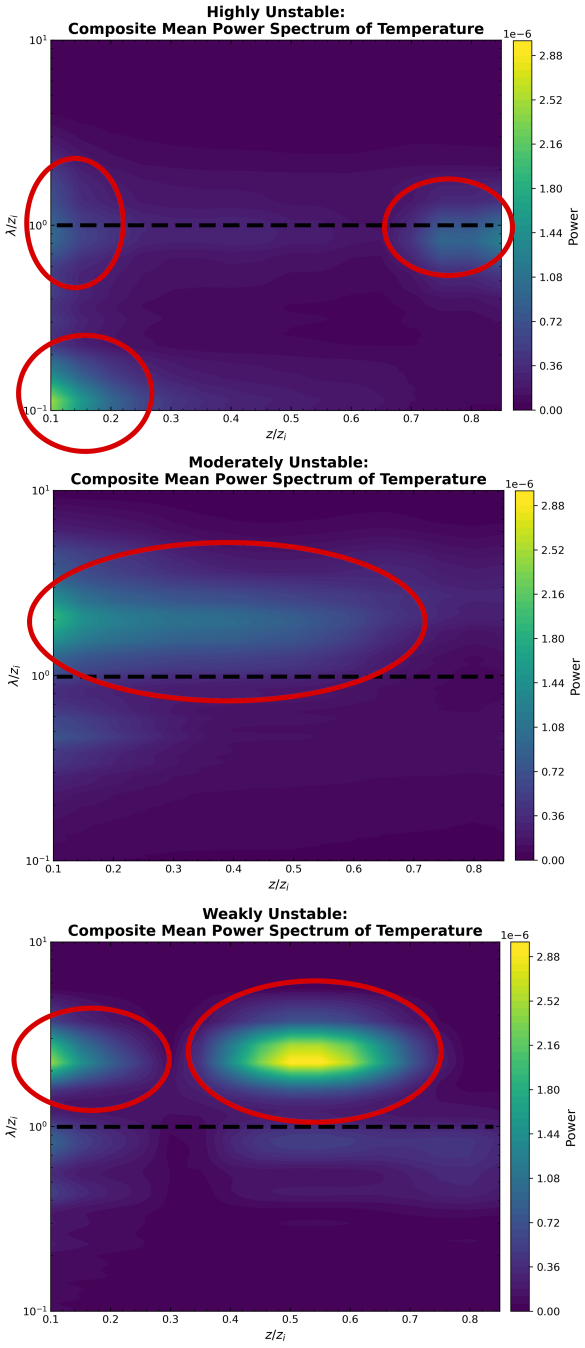

Figure 4.14: Composite mean spectrograms of temperature variance for highly (top), moderately (middle), and weakly unstable (bottom) regimes. The x-axis shows non-dimensional height (z/z_i) and the y-axis shows non-dimensional wavelength (λ/z_i). Color shading indicates spectral power.

Figure 4.15 shows a composite mean power spectra of temperature as a function of normalized height and normalized wavelength for three E_f regimes: 0.0-0.3, 0.3-0.7, and 0.7-1.0. Each panel shows the vertical structure and scale distribution of temperature variance in the CBL, highlighting how spectral characteristics evolve with changes in surface moisture partitioning.

In the low E_f regime (top panel), corresponding to sensible heat dominated conditions, spectral power is broadly distributed at both large and small wavelengths. LSMs have the strongest fluctuations near the surface and power decreases with height. Power is strongest at SSMs below $z/z_i = 0.2$. This indicates strong temperature fluctuations near the surface which is consistent with dry convective conditions, where sensible heat dominates. The vertical decay of power at LSMs suggest that turbulent mixing is weaker aloft and temperature variance is confined to the surface.

As E_f increases to the intermediate range (middle panel), spectral power becomes more dispersed and is concentrated near $\lambda/z_i \approx 1$. This broader distribution indicates mixing throughout the height of the CBL. The balanced surface energy partitioning under these conditions supports deeper and more coherent scalar structures.

The high E_f regime (bottom panel) exhibits the strong spectral power at larger scales at the low to mid-CBL. Latent heat flux dominates in this regime, indicating large-scale mixing throughout the boundary layer.

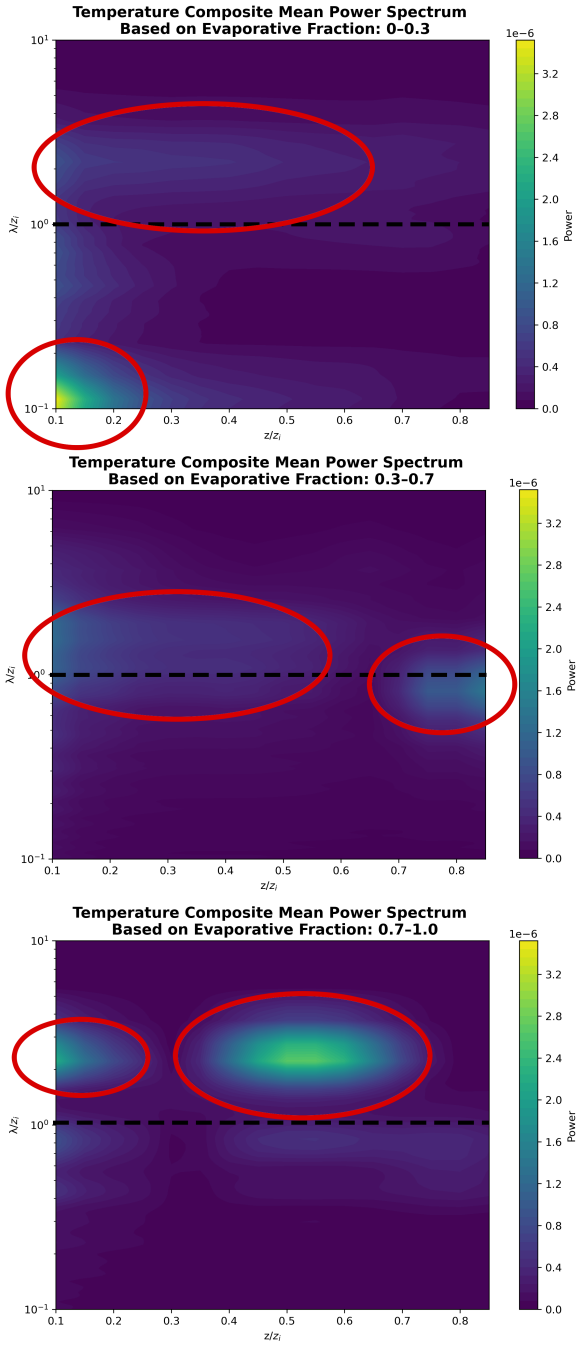

Figure 4.15: Composite mean spectrograms of temperature fluctuations based on dominant modes of E_f, ranging from (top) 0 to 0.3, (middle) 0.3 to 0.7, and (bottom) 0.7 to 1.0.

4.4.3 Moisture Spectral Analysis by Stability Regime

Figure 4.16 shows composite mean spectrograms of water vapor mixing ratio for highly, moderately, and weakly unstable conditions. As in Figure 4.14, these plots display spectral energy as a function of z/z_i and λ/z_i, providing insight into the vertical distribution and dominant scales of moisture variability within the CBL.

Humidity spectra in highly unstable regimes exhibit the lowest spectral energy across all regimes with weak variance, especially in the lower levels of the ABL. However, compared to temperature, spectral power is more concentrated in the lower CBL, and large-scale energy is less prominent. This indicates that moisture transport is more surface-confined, despite the enhanced turbulence under strongly convective conditions.

In moderately unstable cases, humidity variance shows slightly reduced vertical extent, with most spectral power confined below $z/z_i = 0.4$ and at small wavelengths. The absence of larger-scale energy supports the idea that convective structures are shallower and less coherent, limiting upward moisture transport.

Humidity in weakly unstable cases displays the highest spectral energy. Power is confined to the lowest part of the boundary layer and predominantly at short wavelengths, highlighting minimal vertical transport. This reflects the combined effects of low buoyant production and stronger background shear, which inhibit moisture mixing within the CBL.

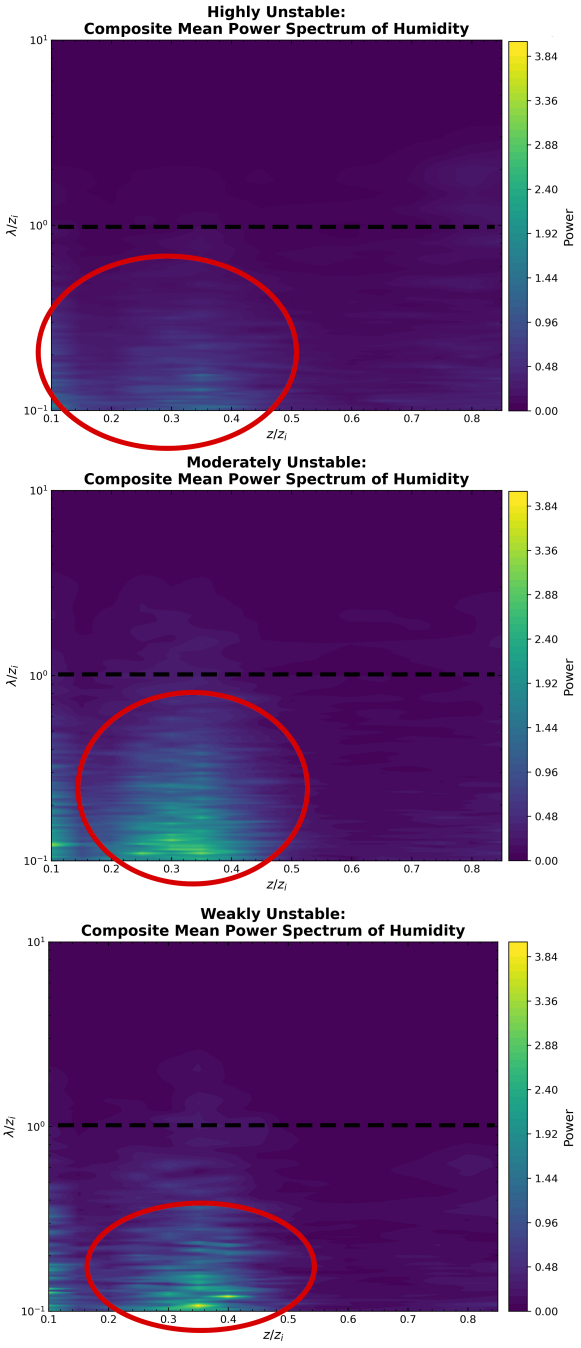

Figure 4.16: Composite mean spectrograms of humidity fluctuations for highly (top), moderately (middle), and weakly unstable (bottom) cases, as in Figure 4.14.

Figure 4.17 shows a composite mean power spectra of humidity as a function of normalized height and normalized wavelength for three E_f regimes: 0.0-0.3, 0.3-0.7, and 0.7-1.0. Each panel shows the vertical structure and scale distribution of humidity variance in the CBL, highlighting how spectral characteristics evolve with changes in surface moisture partitioning.

In the low E_f regime (top panel), corresponding to sensible heat dominated conditions, spectral power is concentrated at smaller vertical scales ($\lambda/z_i < 1$) and lower elevations ($z/z_i < 0.5$). The lack of power at larger scales and higher altitudes suggests that humidity fluctuations are confined near the surface and dominated by smaller, less-organized eddies. This is consistent with dry convective conditions where latent heat flux, and thus moist thermals, play a limited role in boundary layer mixing.

As E_f increases to the intermediate range (middle panel), spectral power becomes more dispersed and extends to slightly larger wavelengths and higher altitudes. This broader distribution indicates enhanced vertical transport and a greater role for buoyancy-driven uplift of moist air parcels. The balanced surface energy partitioning under these conditions supports deeper and more coherent scalar structures.

The high E_f regime (bottom panel) exhibits the strongest spectral power at smaller scales and lower in the boundary layer, particularly below $z/z_i \approx 0.5$. While strong latent heat fluxes in this moist convective environment are expected to drive deep updrafts, the confinement of spectral energy to lower elevations suggests that humidity fluctuations become rapidly homogenized aloft. This implies that vertical transport is efficient enough to reduce coherent humidity variance at higher levels, leading to diminished spectral signatures in the upper CBL.

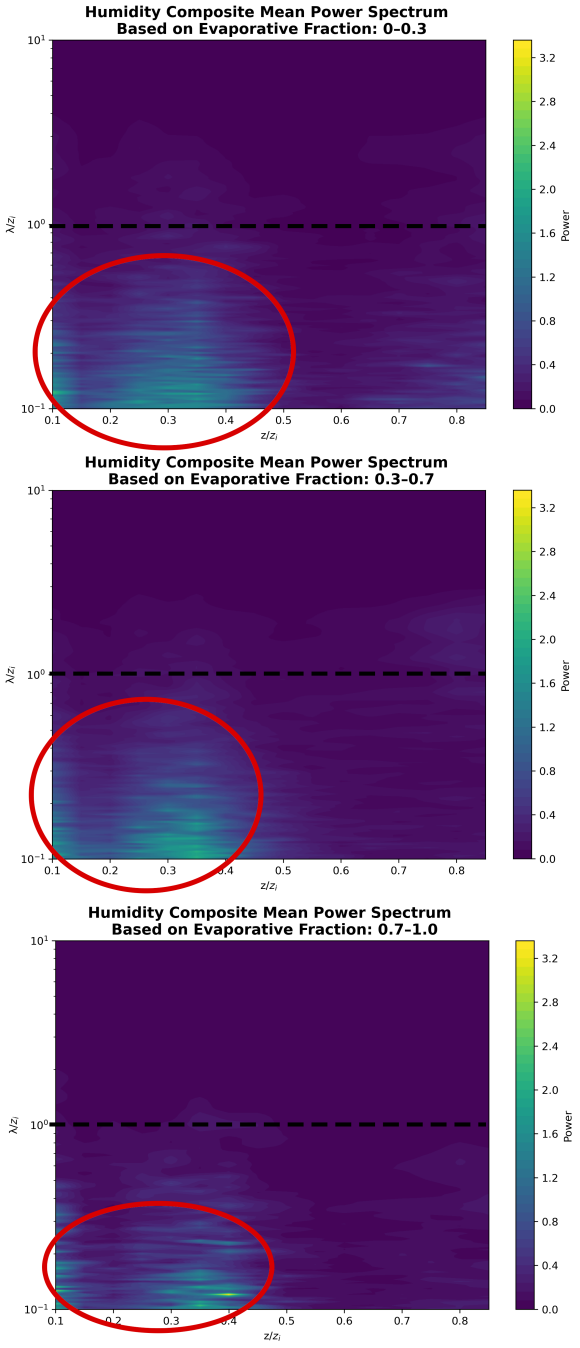

Figure 4.17: Composite mean spectrograms of humidity fluctuations based on dominant modes of E_f, ranging from (top) 0 to 0.3, (middle) 0.3 to 0.7, and (bottom) 0.7 to 1.0.

Collectively, these spectra reveal a systematic shift in the organization of humidity fluctuations with increasing E_f. Scalar transport in the CBL appears to be modulated by large-scale motions whose presence and strength depend on surface flux partitioning. These results support the idea that humidity variance is not only a function of local mixing but is influenced by multiscale coherent structures, with E_f serving as a useful diagnostic for the dominant transport regime.

Chapter 5

Summary and Conclusions

This study investigated the role of large-scale turbulent structures in modulating heat and moisture transport within the CBL, using high-resolution observational data collected at the SGP ARM site during the summer of 2018. Through a composite-based analysis of 107 clear-sky convective cases, the research explored how vertical structure and turbulent variability depend on atmospheric stability, surface flux partitioning, and the presence of organized motions on the scale of the boundary layer depth.

A primary focus was the relationship between scalar transport and large-scale motions (LSMs and VLSMs), which have been shown to organize turbulence and influence flux efficiency in both momentum and scalar fields. While previous work has primarily emphasized their role in momentum transport (e.g., Hutchins & Marusic 2007; Adrian 2007; Saleksky & Anderson 2018), this study extended the analysis to include temperature and humidity.

This research was guided by two central questions:

- **How do moisture-related processes influence vertical profiles of turbulent statistics in the CBL?**

  This study finds that moisture-related processes exert a scale-dependent and distinct influence on vertical profiles or turbulence within the CBL. Analysis of humidity variance and its covariances revealed that moisture is generally more vertically confined than temperature, particularly under weakly and moderately unstable conditions. Humidity fluctuations exhibit greater sensitivity to surface

conditions, with spectral power (Figure 4.17) and variance profiles (Figures 4.4 and 4.5) concentrated near the surface in regimes with low buoyancy production and high shear. The observed correlation between evaporative fraction and the vertical structure of moisture variability supports the interpretation that surface latent heat fluxes, expressed through E_f increases, humidity variance becomes more distributed in height and wavelength, indicating enhanced mixing and vertical coupling between the surface and the entrainment zone.

These results demonstrate that moisture properties, not just the thermal structure, shape the efficiency and scale of turbulent exchange processes in the CBL, particularly by controlling the depth and coherence of scalar structures. Therefore, moisture-related processes not only impact local mixing but also govern the vertical extent of turbulence and entrainment through their interaction with LSMs within the CBL.

- **Do LSMs in the CBL exhibit similar spectral properties for temperature and humidity?**

  Composite spectrograms of temperature and humidity revealed important differences in their dominant turbulent scales. Temperature variance showed enhanced energy at wavelengths on the order of the CBL depth, which is consistent with the influence of LSMs (Figure 4.14), whereas humidity variance was more restricted to smaller wavelengths and confined to lower altitudes (Figure 4.16). This indicates that large-scale turbulent structures exert a stronger organizing influence on temperature than on moisture. The lack of spectral similarity between temperature and humidity suggests different transport mechanisms, challenging the assumption of analogous behavior often made in mixed-layer similarity theory.

Additional results show that the global stability parameter is weakly but negatively correlated with evaporative fraction (Figure 4.1), indicating that convective instability tends to increase when surface fluxes are dominated by sensible heat. This aligns with theoretical expectations and reinforces the importance of surface conditions in modulating CBL turbulence. Spectral analysis of vertical velocity (Figure 4.12) also confirmed that coherent structures are most prevalent and vertically extensive under strong convective conditions, while they become shallower and less organized under moderate or weak instability.

Together, these findings underscore the importance of accounting for both the scale-dependent behavior of scalar transport and the role of coherent turbulent structures when interpreting or modeling CBL dynamics. While this study relied on observational composites, the results motivate further work using large-eddy simulations (LES) and targeted experiments to examine how LSMs interact with entrainment, cloud development, and land-atmosphere coupling. Improved understanding of these interactions can help refine turbulence parameterizations in weather and climate models, particularly under conditions where standard similarity frameworks fall short.

In summary, this research contributes to the growing effort to characterize turbulent processes governing heat and moisture transport within the CBL. By systematically comparing temperature and humidity variance, covariance (Figures 4.2-4.9), and spectral characteristics (Figures 4.11- 4.17) across a range of stability and surface flux regimes, the study reveals key departures from classical scalar similarity assumptions. In particular, humidity variance was found to be more vertically confined than temperature variance, especially under weakly and moderately unstable conditions (Figures 4.16 and 4.17). These regimes exhibited limited vertical mixing and shallow humidity structures, as seen in both variance profiles and composite spectrograms. Spectral

energy in water vapor fluctuations was primarily concentrated at smaller wavelengths and low altitudes, in contrast to temperature, which exhibited broader vertical and spectral distributions (Figures 4.14 and 4.15).

Importantly, the observed dependence of humidity structure on E_f underscores the role of surface moisture availability in shaping CBL turbulence. As E_f increased, vertical moisture variability became more spatially extensive and shifted toward larger scales, suggesting that enhanced latent heating supports deeper, more coherent turbulent structures. However, even in high-E_f regimes, humidity fluctuations tended to homogenize more rapidly aloft, indicating efficient vertical transport but reduced spectral power at higher levels (Figure 4.17). This decoupling between the presence of strong surface fluxes and persistent upper-level variance highlights the important interaction between surface conditions and turbulent transport dynamics.

Overall, these findings challenge the conventional treatment of scalar transport as vertically homogeneous and spectrally uniform. The distinct scale-dependent behavior of moisture suggests that turbulent mixing and entrainment processes are strongly modulated by surface energy partitioning and LSMs. These results reinforce the need for scale-aware modeling approaches that can represent the differential behavior of temperature and humidity in the CBL, particularly in land–atmosphere coupling and cloud initiation contexts.

5.1 Future Work

Future research should continue to explore the role of large-scale structures in scalar transport using both observations and simulations. In particular, LES offers a complementary framework for isolating coherent structures and testing their influence on scalar flux partitioning under controlled conditions. LES studies could also investigate

the sensitivity of temperature and humidity variance spectra to surface flux partitioning, entrainment strength, and boundary-layer growth rates, extending the results presented here.

Expanding the dataset to include additional sites from the DOE ARM network, such as the North Slope of Alaska (NSA) and Eastern North Atlantic (ENA), would allow investigation of scalar transport behavior in contrasting climate regimes. These sites differ substantially in surface energy balance, background humidity, and cloud climatology, providing a valuable testbed for evaluating the generality of findings from the SGP site.

In addition, future work should expand the range of allowable cloud conditions to include cases with greater cloud cover. This study restricted the analysis to near-clear-sky conditions (less than 5% cloud cover) to isolate surface-driven convection. However, shallow clouds are common in many boundary-layer regimes and can still coexist with convective processes. Including cases with modest cloud fractions would allow examination of how cloud presence modifies vertical scalar transport and entrainment, thereby improving the relevance of parameterizations under more representative atmospheric conditions.

Finally, further development of spectrogram-based diagnostics could enable more precise identification of the turbulent scales responsible for scalar transport. Decomposing composite averages of key turbulent statistics, such as $\overline{w'\theta'}$, $\overline{w'q'}$, and $\overline{\theta'q'}$, into scale-dependent contributions may help quantify how flux efficiency varies with wavelength and height, particularly across regimes of differing evaporative fraction or stability.

Reference List

Adrian, R. J., C. D. Meinhart, and C. D. Tomkins, 2000: Vortex organization in the outer region of the turbulent boundary layer. J*ournal of Fluid Mechanics*, **422**, 1–54, https://doi.org/10.1017/S0022112000001580.

Adrian, R. J., 2007: Hairpin vortex organization in wall turbulence. *Physics of Fluids*, **19**, 041301, https://doi.org/10.1063/1.2717527.

ARM | Southern Great Plains. Accessed 19 May 2025, https://www.arm.gov/capabilities/observatories/sgp.

Baldocchi, D. D., B. B. Hincks, and T. P. Meyers, 1988: Measuring Biosphere-Atmosphere Exchanges of Biologically Related Gases with Micrometeorological Methods. *Ecology*, **69**, 1331–1340, https://doi.org/10.2307/1941631.

Beljaars, A. C. M., 1995: The parametrization of surface fluxes in large-scale models under free convection. *Quarterly Journal of the Royal Meteorological Society*, **121**, 255–270, https://doi.org/10.1002/qj.49712152203.

Brown, G. L., and A. S. W. Thomas, 1977: Large structure in a turbulent boundary layer. *The Physics of Fluids*, **20**, S243–S252, https://doi.org/10.1063/1.861737.

Businger, J. A., J. C. Wyngaard, Y. Izumi, and E. F. Bradley, 1971: Flux-Profile Relationships in the Atmospheric Surface Layer.

Cancelli, D. M., M. Chamecki, and N. L. Dias, 2014: A Large-Eddy Simulation Study of Scalar Dissimilarity in the Convective Atmospheric Boundary Layer, https://doi.org/10.1175/JAS-D-13-0113.1.

Cancelli, D. M., N. L. Dias, and M. Chamecki, 2012: Dimensionless criteria for the production-dissipation equilibrium of scalar fluctuations and their implications for scalar similarity. *Water Resources Research*, **48**, https://doi.org/10.1029/2012wr012127.

Choi, T., and Coauthors, 2004: Turbulent exchange of heat, water vapor, and momentum over a Tibetan prairie by eddy covariance and flux variance measurements. *Journal of Geophysical Research: Atmospheres*, **109**, https://doi.org/10.1029/2004JD004767.

Cook, D. R., 2018: Eddy Correlation Flux Measurement System (ECOR) Instrument Handbook. Accessed 22 July 2024, https://doi.org/10.2172/1467448.

Corino, E. R., and R. S. Brodkey, 1969: A visual investigation of the wall region in turbulent flow. *Journal of Fluid Mechanics*, **37**, 1–30, https://doi.org/10.1017/S0022112069000395.

Deardorff, J. W., 1972: Parameterization of the Planetary Boundary Layer for Use in General Circulation Models.

Fedorovich, E., R. Conzemius, and D. Mironov, 2004: Convective Entrainment into a Shear-Free, Linearly Stratified Atmosphere: Bulk Models Reevaluated through Large Eddy Simulations. *Journal of the Atmospheric Sciences*, **61**, 281–295, https://doi.org/10.1175/1520-0469(2004)061<0281:CEIASL>2.0.CO;2.

Fowler, A., and I. Brooks, 2006: Entrainment Zone Definitions: A Large Eddy Study.

Ganapathisubramani, B., N. Hutchins, J. P. Monty, D. Chung, and I. Marusic, 2012: Amplitude and frequency modulation in wall turbulence. *Journal of Fluid Mechanics*, **712**, 61–91, https://doi.org/10.1017/jfm.2012.398.

Head, M. R., and P. Bandyopadhyay, 1981: New aspects of turbulent boundary-layer structure. *Journal of Fluid Mechanics*, **107**, 297–338, https://doi.org/10.1017/S0022112081001791.

Hutchins, N., and I. Marusic, 2007: Evidence of very long meandering features in the logarithmic region of turbulent boundary layers. *Journal of Fluid Mechanics*, **579**, 1–28, https://doi.org/10.1017/S0022112006003946.

Kaimal, J. C., and J. C. Wyngaard, 1990: The Kansas and Minnesota experiments. *Boundary-Layer Meteorology*, **50**, 31–47, https://doi.org/10.1007/BF00120517.

Kaimal, J. C., J. C. Wyngaard, Y. Izumi, and O. R. Coté, 1972: Spectral characteristics of surface-layer turbulence. *Quarterly Journal of the Royal Meteorological Society*, **98**, 563–589, https://doi.org/10.1002/qj.49709841707.

Kim, K. C., and R. J. Adrian, 1999: Very large-scale motion in the outer layer. *Physics of Fluids*, **11**, 417–422, https://doi.org/10.1063/1.869889.

Li, D., and E. Bou-Zeid, 2011: Coherent Structures and the Dissimilarity of Turbulent Transport of Momentum and Scalars in the Unstable Atmospheric Surface Layer. *Boundary-Layer Meteorology*, **140**, 243–262,https://doi.org/10.1007/s10546-011-9613-5.

Long, C., D. Slater, and T. Tooman, 2001: Total Sky Imager Model 880 Status and Testing Results. Accessed 19 May 2025, https://doi.org/10.2172/1020735.

Louis, J.-F., 1979: A parametric model of vertical eddy fluxes in the atmosphere. *Boundary-Layer Meteorology*, **17**, 187–202, https://doi.org/10.1007/BF00117978.

Marusic, I., R. Mathis, and N. Hutchins, 2010: Predictive Model for Wall-Bounded Turbulent Flow. *Science*, **329**, 193–196, https://doi.org/10.1126/science.1188765.

Mathis, R., N. Hutchins, and I. Marusic, 2009: Large-scale amplitude modulation of the small-scale structures in turbulent boundary layers. *Journal of Fluid Mechanics*, **628**, 311–337, https://doi.org/10.1017/S0022112009006946.

Moncrieff, J., R. Valentini, S. Greco, S. Guenther, and P. Ciccioli, 1997: Trace gas exchange over terrestrial ecosystems: methods and perspectives in micrometeorology. *J Exp Bot*, **48**, 1133–1142, https://doi.org/10.1093/jxb/48.5.1133.

Monin, A. S., and A. M. Obukhov: Basic laws of turbulent mixing in the surface layer of the atmosphere.

Morris, V., 2005: Total Sky Imager (TSI) Handbook. Accessed 22 July 2024, https://doi.org/10.2172/1020716.

Newsom, R., 2014: ARM | Derived Wind Profile Data from Doppler Lidar Ready for Review. Accessed 13 March 2025, https://www.arm.gov/news/data/post/26246.

Newsom, R., and R. Krishnamurthy, 2022: Doppler Lidar (DL) Instrument Handbook. Accessed 22 July 2024, https://doi.org/10.2172/1034640.

Newsom, R., R. Bambha, and D. Chand, 2022: Raman Lidar (RL) Instrument Handbook. Accessed 25 January 2025, https://doi.org/10.2172/1020561.

Nichols, W. E., and R. H. Cuenca, 1993: Evaluation of the evaporative fraction for parameterization of the surface energy balance. *Water Resources Research*, **29**, 3681–3690, https://doi.org/10.1029/93WR01958.

Patton, E., P. Sullivan, R. Shaw, J. J. Finnigan, and W. Jeffrey, 2016: Atmospheric Stability Influences on Coupled Boundary Layer and Canopy Turbulence. *Journal of the Atmospheric Sciences*, **73**.

Salesky, S. T., and W. Anderson, 2018: Buoyancy effects on large-scale motions in convective atmospheric boundary layers: implications for modulation of near-wall processes. *Journal of Fluid Mechanics*, **856**, 135–168, https://doi.org/10.1017/jfm.2018.711.

Salesky, S. T., M. Chamecki, and E. Bou-Zeid, 2017: On the Nature of the Transition Between Roll and Cellular Organization in the Convective Boundary Layer. *Boundary-Layer Meteorology*, **163**, 41–68, https://doi.org/10.1007/s10546-016-0220-3.

Sawyer, V., and Z. Li, 2013: Detection, variations and intercomparison of the planetary boundary layer depth from radiosonde, lidar and infrared spectrometer. *Atmospheric Environment*, **79**, 518–528, https://doi.org/10.1016/j.atmosenv.2013.07.019.

Stull, R., 1988: *An Introduction to Boundary Layer Meteorology*.

Turner, D. D., V. Wulfmeyer, L. K. Berg, and J. H. Schween, 2014: Water vapor turbulence profiles in stationary continental convective mixed layers. *JGR Atmospheres*, **119**, https://doi.org/10.1002/2014jd022202.

Wyngaard, J. C., 2010: Turbulence in the Atmosphere. Cambridge University Press, https://doi.org/10.1017/CBO9780511840524.

Wyngaard, J. C., W. T. Pennell, D. H. Lenschow, and M. A. LeMone, 1978: The Temperature-Humidity Covariance Budget in the Convective Boundary Layer.

1 Appendix

Table A.1: Summary of Highly Unstable Cases

Date (YYYYMMDD)	Hour (UTC)	Height (m)	Obukhov Length (m)	$-z_i/L$	w_* (m/s)
20180521	15	576.601	-4.602	125.286	1.376
20180521	16	753.228	-8.110	92.878	1.655
20180521	17	957.087	-11.298	84.716	1.806
20180521	18	1126.969	-12.577	89.605	1.944
20180521	19	1156.449	-12.556	92.105	2.046
20180521	20	1238.142	-7.809	158.560	1.997
20180521	21	1262.625	-11.765	107.324	1.814
20180521	22	1274.117	-17.634	72.252	1.684
20180526	13	1171.439	-15.461	75.768	1.068
20180526	14	1073.257	-12.196	88.004	1.233
20180526	15	1035.533	-8.260	125.374	1.439
20180526	16	1037.531	-9.906	104.741	1.654
20180526	17	971.827	-8.994	108.047	1.810
20180526	18	1008.801	-10.979	91.882	1.957
20180526	19	1139.711	-15.091	75.524	1.916
20180527	13	1177.684	-10.359	113.690	1.248
20180527	14	1151.952	-11.068	104.078	1.615
20180527	15	1125.221	-15.621	72.031	1.797
20180527	19	1228.899	-18.342	66.998	2.150
20180603	12	1346.318	-15.893	84.713	0.658
20180603	13	1352.064	-3.309	408.559	1.151
20180603	14	1306.096	-6.584	198.368	1.389
20180603	15	1225.651	-10.287	119.143	1.622
20180603	18	1272.619	-20.059	63.445	1.880
20180603	19	1250.384	-24.871	50.274	1.874
20180603	20	1238.392	-17.902	69.175	2.102
20180603	21	1220.405	-21.470	56.842	1.760
20180605	13	1625.874	-31.017	52.419	1.235
20180605	14	1703.542	-14.252	119.531	1.670
20180708	13	995.560	-15.354	64.842	0.968
20180708	14	1040.779	-19.976	52.103	1.498
20180708	15	1057.518	-13.985	75.619	1.529
20180711	13	1419.267	-6.109	232.341	1.434
20180711	14	1400.530	-5.420	258.411	1.764
20180711	15	1265.873	-9.358	135.266	1.973
20180711	16	1215.408	-12.467	97.489	2.171
20180711	17	1332.327	-17.418	76.493	2.214
20180713	12	1108.232	-14.710	75.336	0.822

Date (YYYYMMDD)	Hour (UTC)	Height (m)	Obukhov Length (m)	$-z_i/L$	w_* (m/s)
20180713	13	992.562	-10.112	98.161	1.102
20180713	14	1035.533	-7.958	130.127	1.446
20180713	15	1087.747	-10.955	99.288	1.813
20180713	16	1148.705	-9.831	116.848	2.037
20180713	17	1234.395	-12.207	101.124	2.161
20180713	19	1435.506	-14.303	100.363	2.384
20180721	19	1246.886	-24.636	50.613	1.753
20180725	13	1246.137	-4.574	272.444	0.976
20180725	14	1310.093	-5.115	256.134	1.558
20180725	15	1257.379	-2.208	569.501	1.617
20180725	16	1260.627	-5.425	232.359	1.970
20180725	17	1281.612	-6.861	186.809	2.017
20180725	18	1205.915	-6.738	178.973	2.047
20180725	19	1205.915	-5.236	230.316	2.150
20180725	20	1219.406	-8.395	145.251	2.102
20180801	0	1380.793	-15.089	91.508	0.666
20180801	12	1203.666	-7.188	167.456	0.374
20180801	13	1283.861	-13.104	97.976	1.016
20180801	14	1281.362	-9.491	135.012	1.229
20180801	15	1226.151	-10.159	120.694	1.451

Table A.2: Summary of Moderately Unstable Cases

Date (YYYYMMDD)	Hour (UTC)	Height (m)	Obukhov Length (m)	$-z_i/L$	w_* (m/s)
20180518	13	1069.76	-48.24	22.18	1.17
20180518	14	1131.22	-48.98	23.10	1.60
20180518	15	1051.77	-48.00	21.91	1.81
20180518	16	1146.21	-36.76	31.18	2.05
20180518	17	1381.82	-29.90	46.22	2.28
20180518	18	1366.05	-28.37	48.15	2.33
20180518	19	1514.95	-36.59	41.40	2.44
20180518	20	1443.25	-48.25	29.91	2.31
20180518	21	1386.79	-62.21	22.29	2.16
20180518	22	1345.07	-103.85	12.95	1.95
20180521	23	1309.84	-34.53	37.93	1.38
20180526	12	1216.16	-66.10	18.40	0.52
20180527	12	1201.42	-32.25	37.26	0.55
20180527	20	1249.13	-30.74	40.64	2.14
20180527	21	1268.12	-40.80	31.08	1.99
20180527	22	1292.35	-55.85	23.14	1.95
20180603	16	1222.40	-27.20	44.94	1.73
20180603	17	1267.87	-29.10	43.57	1.82
20180615	14	1254.38	-116.19	10.80	1.50
20180615	15	1103.74	-76.93	14.35	1.71
20180615	16	1115.23	-56.44	19.76	1.86
20180615	17	1286.86	-52.17	24.67	2.05
20180615	18	1357.06	-69.13	19.63	2.22
20180711	23	1293.85	-26.85	48.19	1.67
20180713	22	1266.12	-33.68	37.59	1.85
20180721	15	1337.82	-35.34	37.86	1.66
20180721	16	1376.55	-36.16	38.07	1.80
20180721	17	1341.57	-34.87	38.47	1.87
20180721	18	1239.39	-36.15	34.29	1.80
20180721	20	1242.89	-38.62	32.18	1.66
20180721	21	1205.17	-55.12	21.86	1.62
20180721	22	1207.91	-70.71	17.08	1.37
20180721	23	1215.91	-103.18	11.78	1.20
20180801	16	1238.14	-30.89	40.08	1.62
20180801	20	1233.90	-32.84	37.57	1.81
20180801	21	1215.91	-34.41	35.33	1.53

Table A.3: Summary of Weakly Unstable Cases

Date (YYYYMMDD)	Hour (UTC)	Height (m)	Obukhov Length (m)	$-z_i/L$	w_* (m/s)
20180615	13	1278.11	-206.08	6.20	1.14
20180615	22	1264.87	-176.21	7.18	1.83
20180615	23	1308.09	-268.32	4.88	1.63
20180627	15	1270.62	-344.68	3.69	0.76
20180627	16	1225.65	-357.47	3.43	0.85
20180627	17	1161.20	-657.67	1.77	0.76
20180629	14	1150.45	-826.71	1.39	0.67
20180629	15	1162.69	-276.19	4.21	0.95
20180629	16	1059.02	-190.80	5.55	1.17
20180629	17	1089.50	-166.66	6.54	1.16
20180629	18	1184.93	-200.36	5.91	1.20
20180713	00	1439.50	-481.71	2.99	1.02
20180801	19	1218.66	-358.85	3.40	1.82